A&A, 711, A301 (2026)
https://doi.org/10.1051/0004-6361/202659281

Astronomy & Astrophysics

PRISMS: U37126, a very blue ISM-naked starburst at $z = 10.255$ with a nearly 100% Lyman continuum escape fraction

R. Marques-Chaves[1,⋆], J. Álvarez-Márquez[2], L. Colina[2], S. Kendrew[3], Abdurro'uf[4], C. Blanco-Prieto[2,5], L. A. Boogaard[6], M. Castellano[7], K. I. Caputi[8], A. Crespo-Gómez[9], A. Fontana[7], Y. Fudamoto[10], S. Fujimoto[11,12], M. García-Marín[3], Y. Harikane[13], S. Harish[9], T. Hashimoto[14,15], T. Hsiao[16], E. Iani[17], A. K. Inoue[18,19], D. Langeroodi[20], R. Lin[21], J. Melinder[22], L. Napolitano[7], G. Östlin[22], P. G. Pérez-González[2], C. Prieto-Jiménez[2,5], P. Rinaldi[23], B. Rodríguez Del Pino[2], P. Santini[7], Y. Sugahara[18,19], A. Varo-O'Ferrall[2,5], G. Wright[24], and J. Zavala[21]

(Affiliations can be found after the references)

Received 2 February 2026 / Accepted 19 June 2026

ABSTRACT

We present very deep (≈11 hours on-source) JWST/MIRI low-resolution spectroscopy of the rest-frame optical emission of U37126, a UV-bright ($M_{\rm UV} \simeq -20$) mildly lensed ($\mu \simeq 2.2$) galaxy at $z = 10.255$. The continuum emission is well detected in the NIRSpec and MIRI spectra, but no nebular recombination or metal emission lines are observed (EW_0 (Hβ+[O III]) ≤ 300 Å and EW_0 (Hα) ≤ 400 Å at 3σ). Combined with the exceptionally blue UV continuum slope, $\beta_{\rm UV} \simeq -2.9$, and flat Balmer break, these constraints indicate a stellar population dominated by very young and massive stars with a strongly suppressed nebular contribution. Comparisons with synthetic stellar population models indicate that U37126 requires a very high ionizing photon production efficiency, $\log(\xi_{\rm ion}/{\rm Hz\,erg^{-1}}) \simeq 25.75$, and a nearly unity Lyman continuum escape fraction, of $f_{\rm esc} \geq 86\%$ (3σ) based on the Hα flux limit and $f_{\rm esc} = 0.94 \pm 0.06$ derived independently from fitting the spectral energy distribution (SED). The best-fit SED yields a (delensed) stellar mass of $M_\star \simeq 10^{7.8}\,M_\odot$ and a star formation rate SFR $\simeq 10\,M_\odot\,{\rm yr^{-1}}$ (specific SFR $\sim 160\,{\rm Gyr^{-1}}$). Together with its very compact size, $r_{\rm eff} \simeq 61$ pc, this yields a very high stellar mass and SFR surface densities, $\Sigma_{M\star} \simeq 3 \times 10^3\,M_\odot\,{\rm pc^{-2}}$ and $\Sigma_{\rm SFR} \simeq 400\,M_\odot\,{\rm yr^{-1}\,kpc^{-2}}$. Together with the lack of detectable nebular emission, these properties suggest that U37126 is undergoing a so-called interstellar medium-naked starburst phase, possibly driven by an extremely efficient gas-to-star conversion followed by strong feedback that has cleared the remaining gas from its stellar core, which allowed most Lyman continuum photons to escape. Finally, we show that even a small fraction of galaxies such as U37126 (≃3–6%), with an extreme Lyman continuum production and escape, might contribute disproportionately (≃50–100%) to the ionizing photon budget during cosmic reionization.

Key words. galaxies: high-redshift – galaxies: ISM – galaxies: starburst – dark ages, reionization, first stars

1. Introduction

The James Webb Space Telescope (JWST) fundamentally reshapes our understanding of galaxy formation in the early Universe by enabling the detection and detailed characterization of the first galaxies within the first few hundred million years after the Big Bang (e.g., Castellano et al. 2022; Curtis-Lake et al. 2023; Harikane et al. 2023; Pérez-González et al. 2023; Carniani et al. 2024; Castellano et al. 2024; Harikane et al. 2024; Napolitano et al. 2025; Chemerynska et al. 2026; Naidu et al. 2026). Deep NIRCam imaging and NIRSpec spectroscopy provide unprecedented access to the rest-frame ultraviolet (UV) and optical emission of galaxies at redshifts $z \gtrsim 7$, while MIRI extends such studies to even higher redshifts. Together, JWST observations now robustly constrain the physical properties of the earliest galaxies that were previously inaccessible, including their stellar populations, star formation histories, and nebular emission (e.g., Álvarez-Márquez et al. 2024; Bunker et al. 2023; Fujimoto et al. 2024; Álvarez-Márquez et al. 2025; Helton et al. 2026; Zavala et al. 2025; Donnan et al. 2026; Roberts-Borsani et al. 2026; Tang et al. 2026).

The UV continuum slope, $\beta_{\rm UV}$ ($f_\lambda \propto \lambda^{\beta_{\rm UV}}$), is a widely used spectral diagnostic for the physical conditions in star-forming galaxies. Prior to JWST, observations established that typical star-forming galaxies at $z \gtrsim 2$ exhibit relatively blue UV slopes ($\beta \simeq -2$) and that the UV continua become systematically bluer toward higher redshifts and fainter UV luminosities (e.g., Bouwens et al. 2012; Finkelstein et al. 2012; Bouwens et al. 2014; Bhatawdekar & Conselice 2021). These trends are generally interpreted as reflecting lower dust attenuation and younger stellar populations in early galaxies. Recent JWST observations have extended these measurements even above $z > 10$ with improved precision, revealing an increasing prevalence of very steep UV slopes among the earliest galaxies (e.g., Topping et al. 2022; Cullen et al. 2023, 2024; Morales et al. 2024; Topping et al. 2024a; Dottorini et al. 2025; Messa et al. 2025; Saxena et al. 2026).

While moderately blue $\beta_{\rm UV}$ can readily be produced by the hot massive stars expected in young stellar populations, it is considerably more challenging to achieve very steep slopes ($\beta \lesssim -2.6$). It also requires additional physical conditions. At the young ages ($\lesssim$10 Myr) necessary to generate such intrinsically blue stellar continua, nebular emission powered by ionizing photons typically contributes significantly to the observed spectrum, acting to redden the emergent UV spectrum (e.g., Bouwens et al. 2010). As a result, stellar population models generally predict that UV slopes approaching $\beta \simeq -3$ are rare or unobservable in systems in which ionizing photons are efficiently reprocessed

⋆ Corresponding author: Rui.MarquesCoelhoChaves@unige.ch

by the surrounding gas (e.g., Katz et al. 2025). Extremely blue UV slopes thus indicate conditions in which the contribution of nebular emission to the emergent UV spectrum is strongly suppressed. This naturally occurs when a significant fraction of Lyman continuum (LyC; with >13.6 eV) ionizing photons escape from H II regions before they are reprocessed into nebular line and continuum emission.

Galaxies exhibiting extremely steep UV slopes together with weak nebular emission thus are compelling candidates for systems with exceptionally high LyC escape fractions and enhanced ionizing photon output. This framework was first explored by Zackrisson et al. (2013, 2017), who showed that the combination of steep UV slopes and weak rest-optical emission lines provides a powerful means of identifying strong LyC emitters. This has the advantage of not only selecting sources with very high LyC $f_{\rm esc}$, but also with exceptionally high ionizing photon production efficiencies, $\xi_{\rm ion} = Q_{\rm H}/L_{\rm UV}$, where $Q_{\rm H}$ is the hydrogen-ionizing photon production rate, and $L_{\rm UV}$ is the UV luminosity. Such high $\xi_{\rm ion}$ values are expected in very young stellar populations that are required to reproduce extremely steep UV continuum slopes.

Nevertheless, and with a few exceptions, (Marques-Chaves et al. 2022; Kim et al. 2023), confirmed that low-redshift LyC emitters exhibit only moderately blue $\beta_{\rm UV}$ (Chisholm et al. 2022) and generally strong nebular emission lines, with rest-frame Hβ equivalent widths exceeding >150 Å (e.g., Izotov et al. 2016, 2018; Flury et al. 2022). Only recently, JWST started to reveal a rare but non-negligible population of $z > 6$ sources with extremely blue UV slopes and weak nebular emission lines (Topping et al. 2022; Hainline et al. 2024; Donnan et al. 2025; Yanagisawa et al. 2025), often with inferred LyC escape fractions well above $f_{\rm esc} > 50\%$ (e.g., Giovinazzo et al. 2026).

We present the discovery of another such system, UNCOVER-37126 at $z = 10.255$ (hereafter U37126), which was previously identified by Atek et al. (2023) and was spectroscopically confirmed by Fujimoto et al. (2024). Leveraging ultra-deep JWST/MIRI spectroscopy of its rest-frame optical emission, together with ancillary NIRCam imaging and NIRSpec spectroscopy, we show that U37126 exhibits an extremely steep UV continuum slope and a nondetection of nebular emission lines, consistent with a LyC escape fraction close to unity. The paper is organized as follows. Section 2 presents the MIRI, NIRCam, and NIRSpec observations. Section 3 describes the observational results, which are discussed in Section 4. Finally, Section 5 summarizes our conclusions. Throughout this work, we use a concordance cosmology with $\Omega_{\rm m} = 0.31$ and $H_0 = 67.7\,{\rm km\,s^{-1}\,Mpc^{-1}}$ (Planck Collaboration VI 2020).

2. JWST observations and data reduction

U37126 was observed with the Low Resolution Spectrograph (LRS; Kendrew et al. 2015) of the Mid-InfraRed Instrument (MIRI; Rieke et al. 2015; Wright et al. 2015, 2023) on 7–8 November 2025 as part of the PRImordial galaxy Survey with MIRI Spectroscopy at $z \sim 10$ (PRISMS; program ID 8051; PIs: J. Álvarez-Márquez & L. Colina; Álvarez-Márquez et al. 2026). These observations provide a spectral coverage between a wavelength range of 4.80–14.0 µm using a 0.″51 × 4.″7 slit, that is, from $\lambda_{\rm rest} \simeq 0.43$–$1.20$ µm in the rest frame, and a spectral resolution of $R \sim 100$. The total on-source integration time was 39 696 s (≃11.0 h), obtained using a customized four-point dither strategy repeated over 12 dithers. The target acquisition was made using the F560W filter on a GAIA DR3 reference star.

The data reduction followed Álvarez-Márquez et al. (2026). Briefly, we used version 1.20.2 of the JWST calibration pipeline and CRDS context `jwst_1464.pmap`, following the standard MIRI LRS procedures (Bushouse et al. 2025) with additional custom steps to optimize background subtraction and artifact removal. These included wavelength masking, master and residual background subtraction, and sigma clipping to mitigate detector artifacts and cosmic-ray residuals. The final combined 2D spectrum and 1D extracted spectrum were produced using the pipeline stage 3, with the 1D spectrum extracted using a 0.″44 aperture and corrected for aperture losses using the standard JWST reference files (`jwst_miri_apcorr_0017.fits`; for more details, see Álvarez-Márquez et al. 2026).

In addition to the MIRI LRS observations, NIRCam imaging and NIRSpec spectroscopy of U37126 are publicly available as part of the UNCOVER project[1]. NIRCam photometry, combining medium- and broadband filters from F070W to F480M, was taken from the UNCOVER DR3 SUPER catalog (Suess et al. 2024; Weaver et al. 2024). NIRSpec Micro-Shutter Assembly (MSA) spectroscopy, obtained with the low-resolution PRISM ($R \sim 100$), was taken from the UNCOVER data release 4 (Bezanson et al. 2024). We used the fully reduced and calibrated NIRSpec spectrum (≃4.4 hours on-source) published by Fujimoto et al. (2024). Finally, we adopted the updated gravitational magnification from the UNCOVER DR4, $\mu = 2.19 \pm 0.05$ (Furtak et al. 2023; Price et al. 2025).

To place all JWST observations of U37126 on a consistent relative flux scale, we first computed synthetic NIRSpec photometry convolving the NIRSpec spectrum with the filter transmission functions of all medium- and broadband NIRCam filters in which the source was significantly detected (≥3σ; F150W–F480M) and compared it to the corresponding NIRCam photometry. This yielded a scaling factor of ≃1.41, which was applied to the NIRSpec spectrum. For the MIRI LRS spectrum, we computed synthetic photometry over the common spectral range $\lambda_{\rm obs}$ = 4.85–5.30 µm, where the continuum is significantly detected in NIRSpec and MIRI. The flux densities between the two spectra in this region are consistent, and we therefore applied no additional scaling to the MIRI LRS spectrum. Figure 1 shows the combined NIRSpec and MIRI spectra together with the NIRCam photometry.

3. Results

U37126 was first identified by Atek et al. (2023) as a photometric redshift candidate at $z_{\rm phot} = 10.60^{+0.21}_{-0.31}$ based on NIRCam photometry (ID: 39074). A spectroscopic redshift of $z_{\rm spec}$ = 10.255 ± 0.001 was subsequently reported by Fujimoto et al. (2024) based on the unambiguous detection of the Lyα break. A tentative detection of the N III] λ1750 emission line was also discussed by Fujimoto et al. (2024), but we found no significant emission at the reported wavelength, nor evidence of any other rest-frame UV or optical emission lines in the NIRSpec and MIRI spectra (Fig. 1). We therefore adopted the redshift z = 10.255 ± 0.001 inferred from the Lyα break throughout this work. Finally, U37126 was recently observed in the far-infrared with ALMA, but neither dust continuum emission nor [O III] 88 µm line emission was detected, yielding upper limits of $\log(M_{\rm dust}/M_{\odot}) < 6.06$ and L([O III] 88 µm) $< 2\times10^{8}\,L_{\odot}$, respectively (Algera et al. 2025).

[1] https://jwst-uncover.github.io/

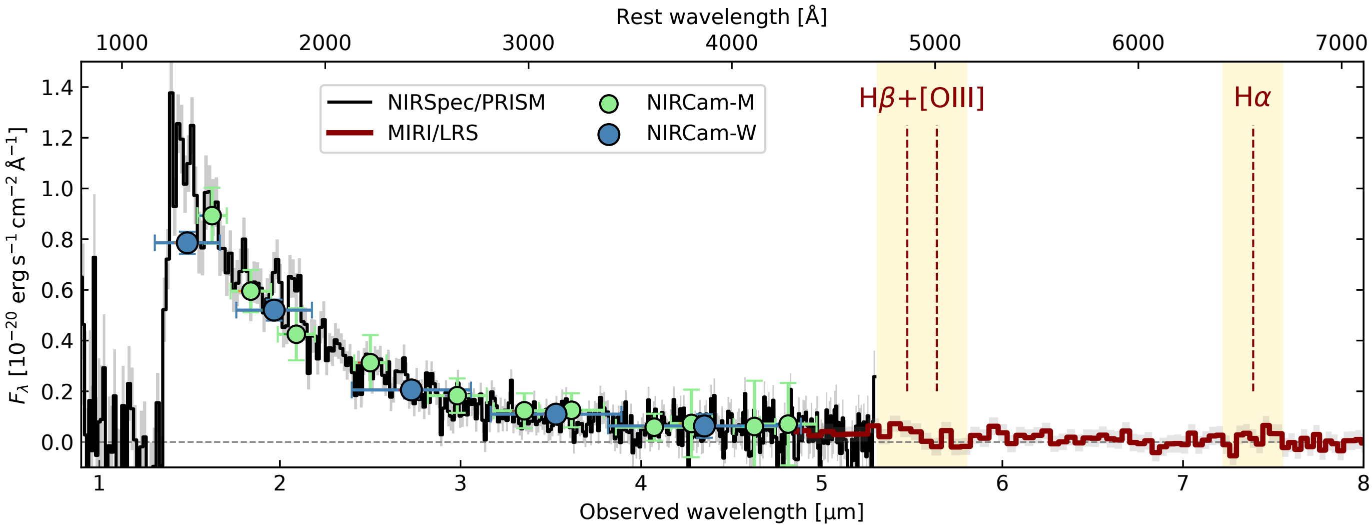

Fig. 1. NIRSpec/PRISM (black) and MIRI/LRS (red) spectra of U37126 with the 1σ uncertainties shown in gray. The expected locations of the main rest-frame optical emission lines, Hβ, [O III] $\lambda\lambda$4960,5008, and Hα, are indicated with dashedred lines. NIRCam photometry from broad- and medium-band filters is overplotted in blue and green, respectively.

3.1. Spectral properties from NIRSpec, NIRCam, and MIRI

The $\beta_{\rm UV}$ was measured using several independent methods based on NIRSpec and NIRCam. We first fit the NIRSpec/PRISM spectrum over a broad and continuous rest-frame window, 1400–3600 Å, thereby excluding regions that might be affected by intergalactic medium (IGM) absorption blueward of 1400 Å and by the Balmer break at longer wavelengths. A power-law fit using `lmfit` (Newville et al. 2025) yielded $\beta_{\rm UV} = -2.79 \pm 0.07$. We then adopted the continuum windows defined by Calzetti et al. (1994), which avoid ISM absorption features, stellar P-Cygni profiles, and nebular emission lines. To remain consistent with the above criteria, we restricted the fit to windows at $\lambda_{\rm rest} \geq 1400$ Å, obtaining $\beta_{\rm UV} = -2.83 \pm 0.09$. As an alternative spectral diagnostic, we fit a first-order polynomial to the wavelength intervals 2180–2220 Å and 2780–2820 Å following Leitherer et al. (1999). This method yielded $\beta_{\rm UV} = -3.05 \pm 0.16$. Finally, we used the NIRCam broadband photometry in F200W and F277W, which sample the rest-frame range $\lambda_{\rm rest} \simeq 1800$–2500 Å. From this, we obtained $\beta_{\rm UV} = -2.86 \pm 0.20$. Taken together, these independent diagnostics consistently indicate that U37126 shows a steep UV continuum slope, all with $\beta_{\rm UV} \lesssim -2.7$. Taking the simple average of these measurements, obtained from different spectral regions and instruments (NIRSpec and NIRCam), and adopting their standard deviation as the uncertainty, we derived a fiducial UV slope of $\beta_{\rm UV} = -2.88 \pm 0.10$.

Another key spectral diagnostic is the strength of the Balmer break, which is sensitive to the age of the stellar population and to the relative contribution of nebular emission. For consistency and to facilitate a direct comparison with the stellar population models discussed next in Section 3.2, we estimated the Balmer break strength of U37126 from the NIRSpec spectrum as the flux density ratio (in F_ν) between $\lambda_{\rm rest} = 4200$ Å and $\lambda_{\rm rest} = 3400$ Å, measured within spectral windows of width $\Delta\lambda_{\rm rest} = 400$ Å. We find a ratio of $F_\nu^{4200\,\text{Å}}/F_\nu^{3400\,\text{Å}} = 0.86 \pm 0.21$. For comparison, using the observed NIRCam photometry in the F356W and F444W filters, which sample the emission shortward and longward of the Balmer break, respectively, we derived a consistent flux density ratio of $F_\nu^{\rm F444W}/F_\nu^{\rm F356W} = 0.88 \pm 0.08$. As discussed further in Section 3.2, the inferred Balmer break strength rules out single-burst stellar populations older than $\gtrsim$6 Myr and continuous star formation histories with ages $\gtrsim$16 Myr.

Finally, we analyzed the MIRI/LRS spectrum. At the redshift of U37126 ($z = 10.255$), the Hβ, [O III] $\lambda\lambda$4960,5008, and Hα emission lines are expected at $\lambda_{\rm obs} = 5.47$ μm, 5.64 μm, and 7.39 μm, respectively, but none of them are significantly detected (Fig. 1)[2]. We estimated their upper flux limits by measuring the root mean square (rms) of the spectrum within a rest-frame window of $\Delta\lambda = 300$ Å centered on the expected position of each line (yellow regions in Figure 1), and we adopted the MIRI/LRS instrumental resolutions of $R \simeq 49$ and $R \simeq 89$ for [O III] and Hα, respectively (Kendrew et al. 2015), that is, we assumed that the emission lines are unresolved. We also considered an intrinsic [O III] 5008/4960 ratio of 2.98 (Osterbrock & Ferland 2006).

Under these assumptions, we derived 3σ limits of F([OIII] λ5008) $\leq 6.6 \times 10^{-19}$ erg s^{-1} cm^{-2} and F(Hα) $\leq 6.9 \times 10^{-19}$ erg s^{-1} cm^{-2}. The continuum emission is significantly detected in the MIRI/LRS ranges $\lambda_{\rm obs} = 4.8$–5.6 μm (37.2 ± 4.1 nJy) and 5.85–6.73 μm (26.1 ± 5.3 nJy), while no significant signal is observed at $\lambda_{\rm obs} \geq 7.0$ μm ($\leq$28 nJy at 3σ). We estimated the continuum emission at the wavelengths of [O III] λ5008 and Hα from the best-fit spectral energy distribution (SED, Section 3.3), finding continuum flux densities of $\simeq$35.8 nJy and $\simeq$27.7 nJy, respectively. These values imply 3σ rest-frame equivalent-width limits under EW_0([O III] λ5008) $\leq$ 174 Å and EW_0(Hα) $\leq$ 400 Å. For Hβ, we assumed case-B recombination with an intrinsic line ratio of $I_{\rm H\alpha}/I_{\rm H\beta} = 2.78$, assuming $T_e = 1.5 \times 10^4$ K and $n_e = 10^3$ cm^{-3} (Luridiana et al. 2015). This yielded an upper limit of F(Hβ) $\leq 2.5 \times 10^{-19}$ erg s^{-1} cm^{-2} and EW_0(Hβ) $\leq$ 64 Å. We emphasize that the Hβ flux and equivalent-width limits are dependent on the assumed case-B recombination conditions. These measurements are summarized in Table 1.

Finally, we briefly examined the spectral region around Lyα. Figure 2 shows the rest-frame Lyα break of U37126, and for comparison, that of MACS0647-JD (Heintz et al. 2024), a star-forming galaxy at a similar redshift ($z = 10.170$) and with comparable global properties (e.g., stellar mass and star formation

[2] The reduced NIRSpec spectrum (v4) from the Dawn JWST Archive extends up to $\lambda_{\rm obs} \simeq 5.5$ μm, but Hβ is not detected either.

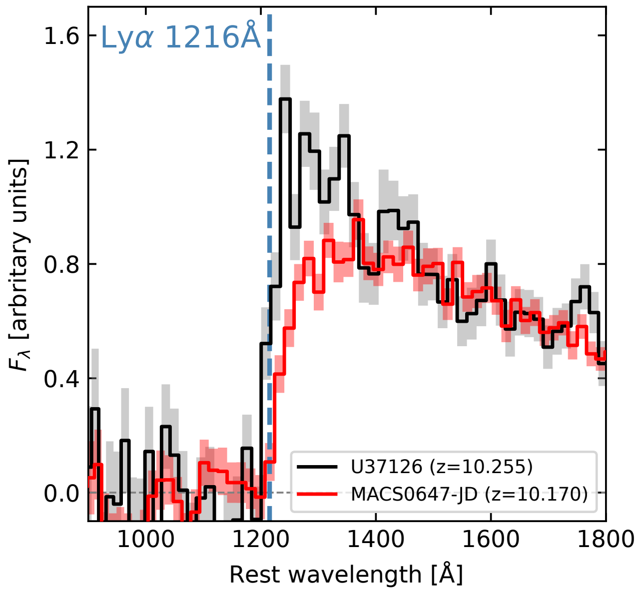

Fig. 2. Comparison of the rest-frame Lyα break of U37126 (black) with that of MACS0647-JD (z = 10.170), which shows a strong damped Lyα absorption feature ($N_{\rm HI} \simeq 2.5 \times 10^{22}$ cm^{-2}, Heintz et al. 2024).

rate). MACS0647-JD exhibits a strong damped Lyα absorption feature, corresponding to a neutral hydrogen column density of $N_{\rm HI} \simeq 2.5 \times 10^{22}$ cm^{-2} (Heintz et al. 2024). In contrast, U37126 shows a very sharp Lyα break, suggestive of a low H I column density along the line of sight. A recent analysis of U37126 by Mason et al. (2026) modeled the Lyα break using the low-resolution PRISM spectrum and inferred a neutral hydrogen column density of $\log(N_{\rm HI}/{\rm cm}^{-2}) = 19.2 \pm 1.5$. Although formally higher than the optically thin limit for LyC escape ($N_{\rm HI} \lesssim 2 \times 10^{17}$ cm^{-2}), the large uncertainty remains statistically consistent with a very high escape fraction at $\sim$1.3σ level.

3.2. Predictions from synthetic stellar models

We compare the observed spectral properties derived in Section 3.1 with predictions from synthetic stellar population models. We adopted the Binary Population and Spectral Synthesis models (BPASS v2.2.1; Stanway & Eldridge 2018), using their default IMF with a slope of −2.35 and an upper mass cutoff of 300 M$_\odot$ (`imf135_300`). We assumed a metallicity Z = 0.003 ($Z/Z_\odot \simeq 0.15$ for $Z_\odot = 0.02$), consistent with values reported for galaxies of comparable $M_{\rm UV}$ at similar redshifts (e.g., Stiavelli et al. 2023; Boyett et al. 2024; Hsiao et al. 2024; Álvarez-Márquez et al. 2025; Helton et al. 2026). Predictions for additional metallicities, from solar to $Z/Z_\odot$ = 0.5%, are presented in Appendix A (Figures A.1–A.4, respectively).

We considered instantaneous-burst and constant star formation histories, with ages from 1 to 100 Myr. For each model, we computed the ionizing photon production rate $Q_{\rm H}$ and predicted the associated nebular continuum emission using `PyNeb` (Luridiana et al. 2015). We assumed nebular conditions with $T_e = 1.5 \times 10^4$ K and $n_e = 10^3$ cm^{-3} that are expected at very high redshifts (e.g., Isobe et al. 2023), and we included free–free and free–bound emission by H and He, and the two-photon continuum of H. Hydrogen recombination-line luminosities (e.g., Hα) were obtained using the coefficients from Osterbrock & Ferland (2006). We additionally included the contribution of the Hγ and Hδ emission lines, as these are sampled by the spectral regions used to infer the Balmer break strength ($F_\nu^{4200\,\text{Å}}/F_\nu^{3400\,\text{Å}}$, see next). The total emergent spectrum is then given by $F_{\rm total} = F_{\rm stellar} + (1 - f_{\rm esc}) \times F_{\rm nebular}$, where the factor $(1 - f_{\rm esc})$ accounts for the ionizing escape fraction, that is, LyC photons not reprocessed into nebular emission. We also assumed negligible dust attenuation given the extremely steep UV slope.

For each model and $f_{\rm esc}$, we measured the UV slope, Balmer-break strength, and EW_0 (Hα) using the same method as applied to U37126 (Section 3.1). Figure 3 (top) shows the predicted quantities as a function of age for $f_{\rm esc}$ = 0, 0.5, and 0.9 (red, green, and blue, respectively). Overall, we recover the expected trends already discussed in previous works: increasing $f_{\rm esc}$ suppresses the nebular continuum and line emission, yielding steeper UV slopes and lower EW_0 (Hα) at a fixed age (e.g., Zackrisson et al. 2013, 2017). UV slopes steeper than $\beta_{\rm UV} < -2.7$ necessarily require a substantial escape of ionizing photons, and this is expected to hold regardless of the assumed IMF, metallicity, and age of the underlying stellar population (cf. Katz et al. 2025; Schaerer et al. 2025), and more broadly, for any ionizing source.

The Balmer break, traced here by the flux density ratio $F_\nu^{4200\,\text{Å}}/F_\nu^{3400\,\text{Å}}$, is close to unity for all burst and constant-SFH models at young ages, reflecting the strong contribution of nebular continuum in the $F_\nu^{3400\,\text{Å}}$ but also the emission lines (Hγ and Hδ) to $F_\nu^{4200\,\text{Å}}$, unless $f_{\rm esc}$ is very high (90%, blue). At ages $\gtrsim$6 Myr ($\gtrsim$15 Myr) for single-burst models (constant star formation), the strength of the Balmer break increases with the stellar age, reflecting the rising contribution of lower-mass stars (A-type) to the integrated spectrum (e.g., Kuruvanthodi et al. 2024; Looser et al. 2024; Baker et al. 2025).

The observational constraints for U37126 are overplotted in Fig. 3. They favor stellar populations with very high $f_{\rm esc}$

Table 1. Summary of the properties of U37126. Global quantities have been corrected for lensing magnification.

Property	Value	Uncertainty
RA [J2000]	00:14:21.63	0.1″
Dec [J2000]	−30:21:35.10	0.1″
z	10.255	0.001
μ	2.19	0.05
$M_{\rm UV}$ [AB]	−20.10	0.05
Age [Myr, CSFH]	6.8	1.6
SFR [$M_\odot$ yr^{-1}]	9.6	4.6
$\log(M_\star/M_\odot)$	7.77	0.06
E(B-V) [mag.]	0.01	0.01
$r_{\rm eff}$ [pc]	61	6
sSFR [Gyr^{-1}]	160	80
$\log(\Sigma_{M\star}$ / $M_\odot$ pc^{-2})	3.40	0.10
$\log(\Sigma_{\rm SFR}$ / $M_\odot$ yr^{-1} kpc^{-2})	2.61	0.22
$\beta_{\rm UV}$	−2.88	0.10
EW_0 ([O III] λ5008) [Å]	≤174	(3σ)
EW_0 (Hβ) [Å]	≤64	(3σ)
EW_0 (Hα) [Å]	≤400	(3σ)
L ([OIII] 5008Å) [erg s^{-1}]	≤4.3 × 10^{41}	(3σ)
L (Hα) [erg s^{-1}]	≤4.5 × 10^{41}	(3σ)
$\log(\xi_{\rm ion})$ [Hz erg^{-1}]	25.75	0.09
$f_{\rm esc}$ (LyC) – Hα	≥0.86	(3σ)
$f_{\rm esc}$ (LyC) – SED	0.94	0.06

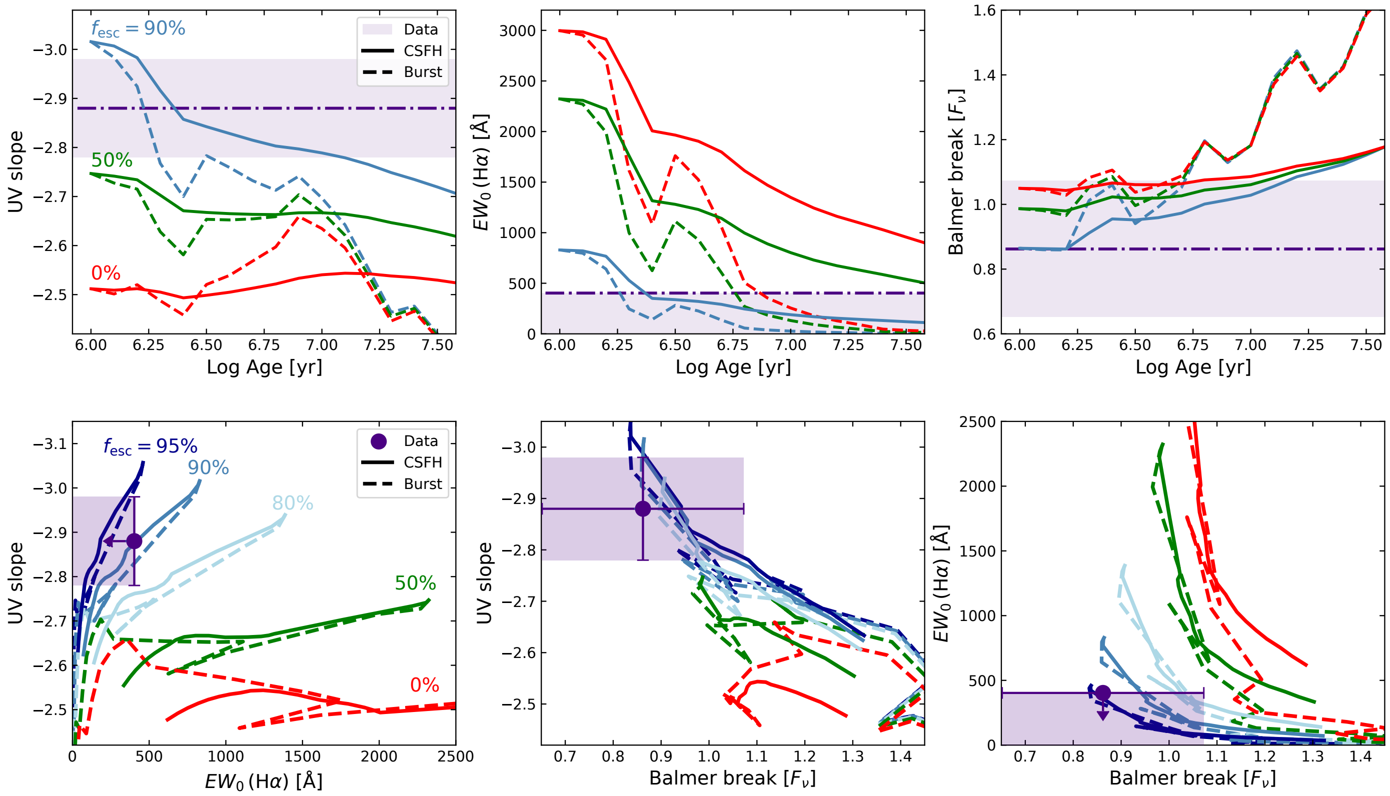

Fig. 3. Predictions from BPASS synthetic stellar and nebular emission models ($Z/Z_\odot \simeq 0.15$, $T_e = 1.5 \times 10^4$ K, and $n_e = 10^3\,\mathrm{cm^{-3}}$) for the UV continuum slope (β_{UV}), EW_0 (Hα), and the Balmer break strength ($F_\nu^{4200\,Å}/F_\nu^{3400\,Å}$) as a function of the age (top) and their combination (bottom). The solid and dashed lines correspond to constant star formation (CSFH) and instantaneous burst models (Burst), respectively. Model sequences are shown for LyC escape fractions f_{esc} ranging from 0% (red) to 90% (blue); additional models with f_{esc} = 80% and 95% are shown in the bottom panels only (light and dark blue, respectively). The dot-dashed violet lines (top) and circles (bottom) indicate the observational constraints for U37126, with the shaded regions representing the 1σ uncertainties, except for EW_0 (Hα), which represents the 3σ upper limit.

along with young ages, ≃2–10 Myr for constant star formation or ≃1–3 Myr for single-burst models. Thus, our results indicate that the lack of nebular emission in the MIRI/LRS spectrum is primarily driven by an exceptionally high f_{esc} and very young stellar populations and not by an evolved population with reduced LyC production. While single stellar population models (dashed red in Fig. 3) with ages >6 Myr can match the observed EW_0(Hα) upper limit, they cannot simultaneously reproduce the observed steep UV slope and weak Balmer break. As a simple estimate, we considered a 5 Myr constant-SFH BPASS model redshifted to z = 10.255 and scaled to match the observed spectrum. This scaled BPASS model, shown in Figure 5 (violet), has $\log(Q_H/\mathrm{s^{-1}}) \simeq 54.4$ (delensed) and a high ionizing photon production efficiency, $\log(\xi_{ion}/\mathrm{Hz\,erg^{-1}}) \simeq 25.75$. For comparison, if we had used the Hα limit assuming $f_{esc} = 0$, we would obtain $\log(\xi_{ion}/\mathrm{Hz\,erg^{-1}}) \leq 25.02$ (2σ), that is, we would underpredict its true ξ_{ion} by >0.73 dex. Together with our upper limit on the Hα luminosity (L(Hα) ≤ $4.5 \times 10^{41}\,\mathrm{erg\,s^{-1}}$, delensed), our results indicate an $f_{esc} \geq 86\%$ at 3σ for U37126, assuming a stellar metallicity of 15% $Z_\odot$. Figure 4 shows the corresponding 3σ limits on the LyC escape fraction derived using the same method across a range of stellar metallicities (0.5% to 100% $Z_\odot$) and gas electron temperatures (1.0–2.5 × 10^4 K). At low metallicities (≲0.15 $Z_\odot$), we find $f_{esc} \geq$ 86–91% (3σ), whereas at higher metallicities (∼0.5–1.0 $Z_\odot$), the limits decrease to $f_{esc} \geq$ 69–80% (3σ). We note, however, that other independent indicators (e.g., β_{UV}) still favor high escape fractions at higher metallicities ($f_{esc} \gtrsim 90\%$; see Figures A.1 and A.2).

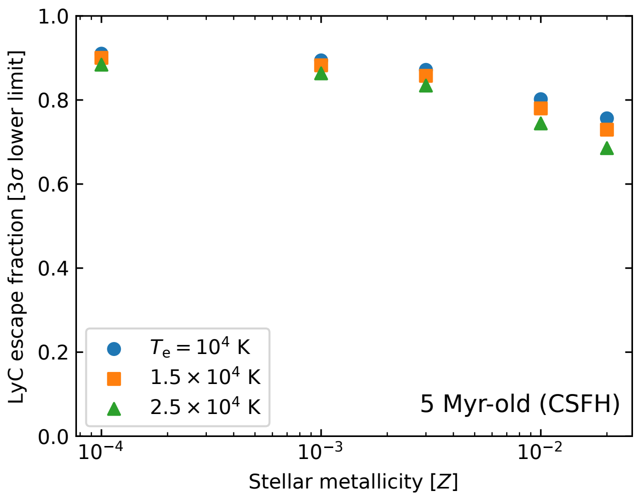

Fig. 4. Limits (3σ) on the Lyman continuum escape fraction derived from the upper limit on the observed (delensed) Hα luminosity as a function of stellar metallicity (from 0.5% to 100% solar) assuming a 5 Myr constant-SFH. Different symbols and colors correspond to assumed gas electron temperatures of 10^4 K (blue), 1.5×10^4 K (orange), and 2.5 × 10^4 K (green).

In summary, our results indicate a high LyC escape fraction that is largely independent of the assumed stellar population properties ($f_{esc} \geq 86\%$ at 3σ for our fiducial model). We emphasize that given the limited observational constraints, these

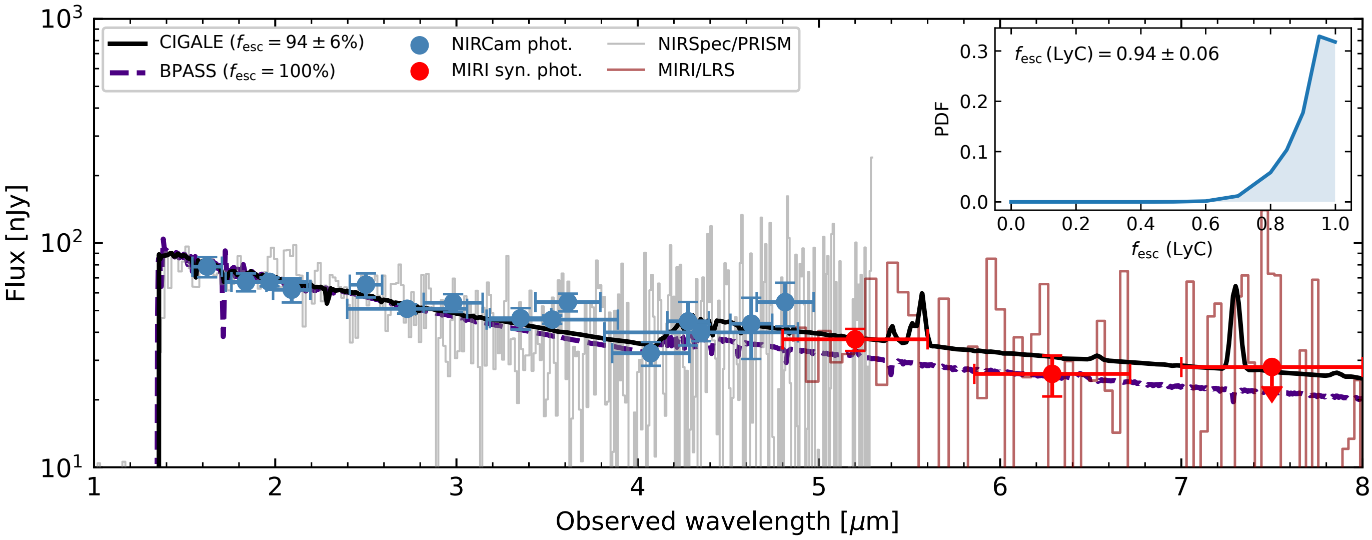

Fig. 5. Best-fit SED of U37126 derived with CIGALE (solid black curve) and a pure stellar 5 Myr old BPASS model (CSFH with $Z/Z_\odot$ = 15%, dashed violet line). The NIRSpec/PRISM and MIRI/LRS spectra are shown in gray and red, respectively, and NIRCam photometric measurements and MIRI/LRS synthetic photometry are indicated by blue and red circles. The inset panel displays the posterior probability density function of the Lyman continuum escape fraction.

conclusions are also somewhat agnostic to the nature of the ionizing source. In particular, regardless of whether the ionizing radiation is dominated by a young stellar population or includes a contribution from an AGN, the combination of a hot ionizing source ($\beta_{UV} \simeq -2.9$) and the lack of detectable nebular emission implies that only a small fraction of ionizing photons is absorbed by the interstellar medium.

3.3. Spectral energy distribution and global properties

We fit the SED using the SpectroPhotometric version of the code CIGALE (V.2022.1; Burgarella et al. 2005; Boquien et al. 2019; Burgarella et al. 2025), incorporating all NIRCam photometry, the NIRSpec/PRISM spectrum, and MIRI/LRS measurements of the [O III] λ5008 and Hα upper flux limits and the continuum emission between λ_{obs} = 4.8–5.6 μm, 5.85–6.73 μm, and >7.0 μm (see Section 3.1). We excluded all observations below λ_{rest} < 1400 Å from the fit since they may be affected by IGM absorption and the effect is not properly handled by CIGALE.

The star formation history (SFH) was modeled assuming constant star formation with ages varying from 1 to 20 Myr in steps of 1 Myr. We adopted stellar population models from Bruzual & Charlot (2003), assuming a Chabrier (2003) IMF and metallicities from $Z/Z_\odot$ = 2–20%. The ionization parameter ranged from $\log(U) = -3.0$ to -1.5 in 0.5 dex steps. We adopted the Milky Way dust extinction law from Cardelli et al. (1989) with R_V = 3.1 as the dust attenuation law for the nebular emission and the Calzetti et al. (2000) for the stellar emission. The color excess of the nebular gas was allowed to vary from 0 to 0.5 mag. The escape of LyC photons was allowed to vary from 0 to 0.999. Finally, we added an uncertainty of 10% to all dataset points to account for cross-calibration systematics between NIRSpec, NIRCam, and MIRI.

Our best-fit SED model (χ^2_ν = 0.64), shown in Figure 5, is characterized by a stellar population with a constant star formation rate SFR = 9.6 ± 4.6 $M_\odot$ yr^{-1} (10 Myr weighted), a stellar mass $\log(M_\star/M_\odot)$ = 7.77 ± 0.06, and an age of 6.8 ± 1.6 Myr (where global properties are corrected for magnification, assuming μ = 2.19). This yields a specific star formation rate sSFR = 160 ± 80 Gyr^{-1}. The color excess is negligible, $E(B-V)$ = 0.01 ± 0.01 mag., as expected given the very steep UV slope of the best-fit model, β_{UV} = −2.85 ± 0.05 (and consistent with our measurements in Section 3.1). The nebular metallicity is found to be $Z/Z_\odot$ = 7.8 ± 7.1%.

The best-fit model also provides a very high LyC escape fraction, f_{esc} = 0.94±0.06 (Figure 5, inset panel), consistent with the results obtained in Section 3.2. Finally, using the demagnified size of r_{eff} = 61 ± 6 pc derived next in Section 3.4, we obtained a stellar mass and SFR surface densities of $\log(\Sigma_{M\star}/M_\odot\,\mathrm{pc}^{-2})$ = 3.40 ± 0.10 and $\log(\Sigma_{SFR}/M_\odot\,\mathrm{yr}^{-1}\,\mathrm{kpc}^{-2})$ = 2.61 ± 0.22, respectively. These values are substantially higher than those of typical star-forming galaxies at high-z (e.g., Morishita et al. 2024) and are instead comparable to those found in young massive star clusters and globular clusters (e.g., Vanzella et al. 2023) and in some of the most extreme sources at the highest redshifts (Castellano et al. 2022; Tacchella et al. 2023; Naidu et al. 2026). These properties are summarized in Table 1.

3.4. Morphology and size

The morphology of U37126 is compact in the NIRCam imaging, as illustrated in the top panels of Fig. 6. To quantify its structural properties, we modeled the light distribution using `PySersic` (Pasha & Miller 2023). `PySersic` performs forward modeling of galaxy morphologies with Sérsic profiles convolved with a supplied point spread function (PSF) and employs a Bayesian framework to explore the posterior distribution of all parameters and their degeneracies.

Empirical PSFs from the UNCOVER DR4 release (Suess et al. 2024; Weaver et al. 2024) are available for all NIRCam bands, but only at a pixel scale of 0.04″ pix^{-1}. Because the short-wavelength NIRCam images (e.g., F150W and F200W) have been resampled in UNCOVER DR4 to a pixel scale of 0.02″ pix^{-1}, we generated PSFs for these bands using STPSF[3] (Perrin et al. 2014). We followed Morishita et al. (2024) and Weibel et al. (2024) and set the `jitter_sigma` parameter

[3] https://stpsf.readthedocs.io/en/latest/

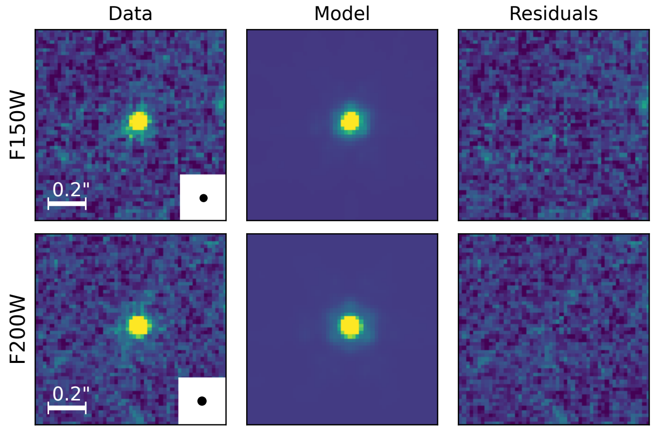

Fig. 6. NIRCam F150W (top) and F200W (bottom) $1'' \times 1''$ cutouts of U37126. The middle and right panels show the Sérsic best-fit models obtained with `PySersic` and the corresponding residuals, respectively. The PSFs are shown in the left panels.

in `WebbPSF` to 0.022, which has been shown to reproduce the observed NIRCam PSFs best.

We fit 2D Sérsic models, allowing the Sérsic index to vary between 0.5 and 6.0, while leaving the total flux, effective radius, ellipticity, and position angle free. Given the significantly higher S/N in the NIRCam broadband filters relative to the medium bands, we restricted our morphological analysis to the broadband imaging alone and also excluded the F444W image for the same reason (low S/N). Each fit was performed on a $1'' \times 1''$ cutout, and all fits were centered on U37126.

For the short-wavelength NIRCam images, we measured effective radii of $r_{\rm eff} = 24 \pm 2$ mas in F150W and $r_{\rm eff} = 22 \pm 2$ mas in F200W, respectively (Figure 6), and a Sérsic index of $n = 1.64 \pm 0.26$. We adopted the F200W value, as this band probes the rest-frame UV at $\simeq$1750 Å. Because U37126 is moderately magnified by A2744, with $\mu = 2.19 \pm 0.05$ (Furtak et al. 2023; Price et al. 2025), we obtained a demagnified radius of $r_{\rm eff} = 61 \pm 6$ pc at $z = 10.255$. At longer wavelengths, the best-fit models yield $r_{\rm eff} \lesssim 0.5$ pix (or $r_{\rm eff} \lesssim 0.02''$). Thus, U37126 appears to be unresolved in the rest-optical with $r_{\rm eff} < 160$ pc (or $<$100 pc after lensing correction).

4. Discussion

4.1. Comparison with other confirmed strong LyC emitters and $z > 6$ candidates

Our results strongly support a scenario in which U37126 produces and leaks large numbers of LyC photons. These constraints are driven by the combination of its extremely steep UV continuum and the nondetection of nebular emission, and indirectly, from the very sharp Lyα break. Although extreme, similar properties have been identified with JWST in a small number of sources at $z \sim 6$–10 (Topping et al. 2022; Hainline et al. 2024; Yanagisawa et al. 2025; Giovinazzo et al. 2026; Jecmen et al. 2026). These galaxies share comparably blue UV continua and unusually weak nebular emission, which indicates very young stellar populations with very high LyC $f_{\rm esc}$. Interestingly, several of these galaxies also show high SFRs within extremely compact morphologies ($r_{\rm eff} < 260$ pc). This results in a very high $\Sigma_{\rm SFR}$, comparable to that inferred for U37126, $\log(\Sigma_{\rm SFR}/{\rm M}_{\odot}\,{\rm yr}^{-1}\,{\rm kpc}^{-2}) \simeq 2.6$, and it is consistent with expectations for strong LyC leakage (Sharma et al. 2017; Naidu et al. 2020).

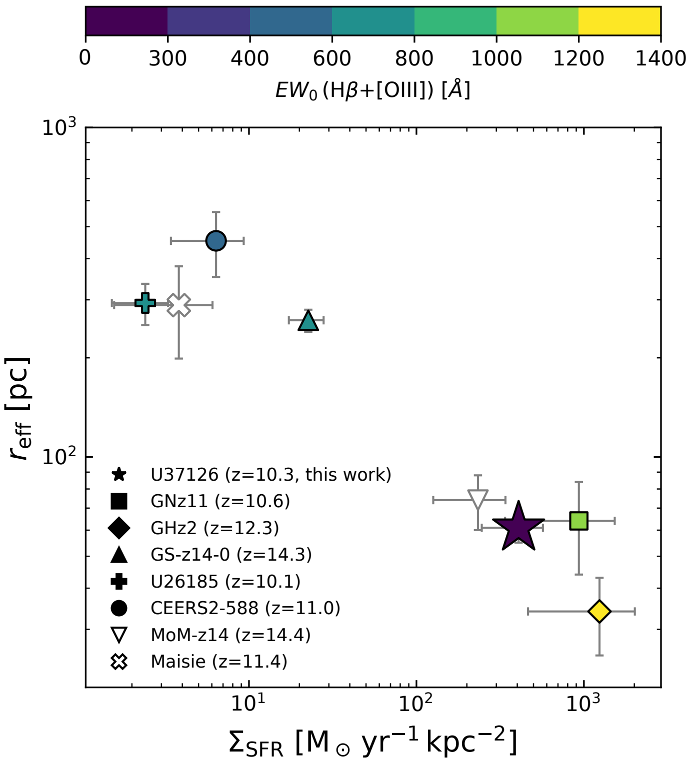

Fig. 7. Effective radius ($r_{\rm eff}$) as a function of star formation rate surface density ($\Sigma_{\rm SFR}$) for galaxies at $z > 10$ with MIRI constraints on EW_0 (Hβ+[O III]) (color-coded, from Castellano et al. 2022; Goulding et al. 2023; Tacchella et al. 2023; Calabrò et al. 2024; Carniani et al. 2024; Álvarez-Márquez et al. 2025; Helton et al. 2026; Zavala et al. 2025; Harikane et al. 2026, and Álvarez-Márquez et al. 2026). The symbols denote individual sources, and the open symbols indicate sources without available EW_0 measurements (Arrabal Haro et al. 2023; Naidu et al. 2026). U37126 (star) occupies the compact high-$\Sigma_{\rm SFR}$ regime, but shows unusually weak nebular emission with EW_0 (Hβ+[O III]) < 296 Å (3σ) compared to other compact systems (e.g., GNz11 and GHz2), consistent with a high LyC escape fraction.

Recent JWST studies have further suggested a dichotomy among galaxies at $z \gtrsim 10$ (Harikane et al. 2025; Roberts-Borsani et al. 2026), separating extended systems with relatively weak emission lines, in some cases, accompanied by Balmer breaks (Harikane et al. 2026; Álvarez-Márquez et al. 2026), which might be undergoing a recent decline in star formation (e.g., Helton et al. 2026), from very compact galaxies ($r_{\rm eff} \lesssim 100$ pc) experiencing recent bursts and exhibiting strong UV and/or optical emission lines (e.g., Bunker et al. 2023; Castellano et al. 2024; Álvarez-Márquez et al. 2025; Zavala et al. 2025). Figure 7 shows the effective radius and star formation rate surface density of the small sample of $z > 10$ sources with MIRI constraints on the rest-optical emission. The color scale encodes the rest-frame equivalent width EW_0(Hβ+[O III]). Compact systems generally occupy the regime of high $\Sigma_{\rm SFR}$ and large equivalent widths. U37126 lies in this compact high-$\Sigma_{\rm SFR}$ regime, but shows unusually weak nebular emission, which is naturally explained by its very high LyC escape fraction.

To further place U37126 in context, we compared its observed properties with those of confirmed LyC emitters at lower redshifts ($z < 4$), where LyC escape can be measured directly. We first note that the majority of known LyC emitters exhibit relatively modest escape fractions and UV slopes $\beta_{UV} > -2.5$ (e.g., Izotov et al. 2018; Steidel et al. 2018; Marques-Chaves et al. 2021; Flury et al. 2022; Kerutt et al. 2024). Only a small subset shows $f_{esc} > 50\%$, and nearly all of them exhibit strong nebular emission, with typical Hβ equivalent widths of ~100−300 Å (de Barros et al. 2016; Izotov et al. 2016; Vanzella et al. 2016; Izotov et al. 2018; Rivera-Thorsen et al. 2019; Flury et al. 2022). An exception is the strong LyC leaker J1316+2614 at $z = 3.6$, which has a measured $f_{esc} \simeq 87\%$, EW_0 (Hβ) $\simeq$ 35 Å, and $\beta_{UV} \simeq -2.6$ (Marques-Chaves et al. 2022) although it is much brighter. It represents the closest known analog to U37126 and to other $z > 6$ strong LyC emitting candidates with steep UV slopes and weak nebular emission.

At face value, the observed high f_{esc} and strong nebular emission in some confirmed strong LyC emitters appear to be at odds with the predictions and with the properties of U37126 (Fig. 3). However, these observations are not necessarily contradictory. The measured f_{esc} in low-z LyC emitters probes LyC escape along the line of sight toward the young stars, whereas nebular emission traces a more global 4π-averaged escape fraction. Strongly anisotropic LyC leakage can therefore result in high apparent f_{esc} values while still producing prominent nebular emission (e.g., Flury et al. 2022; Jaskot et al. 2024a). In addition, LyC flux measurements close to the Lyman limit may be boosted by nebular bound-free emission (Inoue 2010; Simmonds et al. 2024b), potentially leading to an overestimation of the stellar f_{esc}. As recently shown by Izotov et al. (2025), this effect appears to be significant in J1243+4646, the strongest LyC emitter at $z \simeq 0.3$ that is also a strong line emitter ($f_{esc} \simeq 72\%$ and EW_0(Hβ) $\simeq$ 221 Å, Izotov et al. 2018).

These results thus suggest that sources such as U37126, which are characterized by very steep UV slopes with faint nebular emission, may be rare or absent at $z < 4$. However, it remains unclear whether this reflects a genuinely low number density at lower redshifts, possibly due to the specific physical conditions required to form such systems (see Section 4.2), or if they have been systematically overlooked in LyC surveys due to selection effects (e.g., Bergvall et al. 2013), as the confirmation of spectroscopic redshifts generally relies on strong nebular emission.

4.2. Conditions for forming ISM-naked starbursts with a LyC escape fraction of nearly unity

The nature of sources such as U37126 is intriguing because typical starburst galaxies are gas rich and exhibit strong nebular emission. The stringent 3σ upper limits on the equivalent widths, together with the very steep UV continuum and a weak or flat Balmer break strength, indicate that nebular emission is intrinsically weak and that a small fraction of LyC photons at most is being reprocessed by the surrounding gas.

To obtain a rough estimate of the characteristic size of the ionized region associated with U37126, we computed the Strömgren radius,

$$R_S = \left(\frac{3\, Q_H}{4\pi\, \alpha_B\, n_H^2} \right)^{1/3},$$

where $Q_H \approx 10^{54.4}$ s^{-1} (Section 3), n_H is the hydrogen number density of the surrounding gas, and α_B is the case-B recombination coefficient. For typical electron temperatures $T_e \simeq (1\text{–}2) \times 10^4$ K and gas densities $n_H \simeq 10^2\text{–}10^3$ cm^{-3}, we infer Strömgren radii of $R_S \approx 50\text{–}200$ pc. These scales are comparable to or exceed the size of the stellar emission ($r_{eff} \simeq 61$ pc; Section 3.4). Under such extreme conditions, any substantial gas reservoir located within or around U37126 is expected to be efficiently ionized, and therefore, most likely detectable in the NIRSpec and MIRI spectra.

One possible exception is a scenario in which the ionized gas is extremely diffuse, because the line luminosities scale as $L \propto n_e^2$. Even if all LyC photons were fully reprocessed within H II regions, the nondetection of Hα emission might, in principle, be explained by an extremely low electron density ($n_e \lesssim 10^{-2}$ cm^{-3}). However, such conditions are rarely observed and are particularly unlikely for U37126 ($z = 10.255$), given the expected increase in the electron density toward higher redshifts (e.g., Isobe et al. 2023). Moreover, the extreme stellar mass and SFR surface densities of U37126 would instead favor high electron densities (e.g., Reddy et al. 2023a,b). Consistent with this expectation, nearly all sources at $z > 10$ with sizes comparable to that of U37126 ($r_{eff} \approx 61$ pc) exhibit evidence for extremely high gas densities (Harikane et al. 2025), several of them shown in the bottom right corner of Figure 7 (e.g., GNz11 and GHz2). Taken together, the absence of detectable nebular emission in U37126 suggests that the galaxy is largely depleted of its interstellar medium. U37126 thus behaves as an ISM-free starburst, raising the question of how such conditions can be achieved.

One possibility is that during its intense star formation episode, the bulk of the natal gas in U37126 was rapidly and efficiently converted into stars, leaving little residual gas available to absorb and reprocess LyC photons. Dekel et al. (2023) (see also Li et al. 2024) predicted that extremely high gas surface densities ($\Sigma_{gas} \gtrsim 3 \times 10^3\ M_\odot$ pc^{-2}) can lead to the formation of feedback-free starbursts (FFB), in which gas clouds collapse on very short free-fall timescales (~1 Myr). This makes star formation very efficient, since the cloud collapse occurs before the onset of mechanical feedback (e.g., SNe). While the gas surface density of U37126 cannot be measured directly, the observed stellar mass surface density, $\log(\Sigma_{M\star}/M_\odot\ \text{pc}^{-2}) = 3.40 \pm 0.10$, suggests a pre-star formation gas surface density of at least comparable magnitude, thus satisfying the condition for an FFB. Observationally, high star-formation efficiencies have been inferred (>40%; Dessauges-Zavadsky et al. 2025) and predicted (>70%; Marques-Chaves et al. 2024) to explain the strong LyC escape that was directly measured in the strong leaker J1316+2614 at $z = 3.6$ with $f_{esc} \approx 87\%$ and EW_0 (Hβ) $\simeq$ 35 Å (Marques-Chaves et al. 2022).

An alternative but not mutually exclusive scenario is that strong feedback has removed gas and dust from the stellar core of U37126, and potentially to larger distances[4]. In this context, Ferrara et al. (2023) proposed that radiation pressure on dust and gas can drive powerful radiative feedback during super-Eddington phases. These conditions are expected in the early stages of a starburst, when the sSFR exceeds a critical threshold of $\gtrsim$25 Gyr^{-1} (Fiore et al. 2023), which is satisfied in this source ($\simeq$160 Gyr^{-1}). These phases can also facilitate substantial LyC leakage, as shown recently by Ferrara et al. (2025). Furthermore, recent hydrodynamic simulations have shown that strong radiative outflows can only be efficiently launched in very dense systems with high star formation efficiencies, leading simultaneously to strong LyC leakage (Menon et al. 2025). Observational evidence of extreme outflows like these has been reported in a handful of powerful starbursts with an elevated

[4] Given the widths of the NIRSpec/MSA and MIRI/LRS apertures of ≃0.2″ and 0.5″, respectively, within which no nebular emission appears detected. This corresponds to ~0.8 kpc and ~2.1 kpc at $z = 10.25$, i.e., much larger than the size of U37126 ($r_{eff} \simeq 61$ pc).

sSFR (Crespo Gómez et al. 2025; Marques-Chaves et al. 2026), including in confirmed low-z LyC emitters (e.g., Komarova et al. 2025). However, these systems still exhibit intense nebular emission, unlike U37126.

In summary, the absence of detectable gas in U37126 might reflect an evolutionary sequence in which exceptionally efficient star formation rapidly consumes the natal gas, followed by intense feedback that expels the remaining material, including dust, from the stellar core. In the absence of subsequent gas accretion, U37126 might then evolve rapidly into a post-starburst or recently quenched system, such as the systems recently identified by JWST at high-z (e.g., Looser et al. 2024).

4.3. Implications for cosmic reionization

The discovery of powerful ionizing sources such as U37126 has important implications for cosmic reionization. The ionizing photon budget is commonly expressed through the comoving ionizing emissivity, $\dot{n}_{\rm ion}$, defined as $\dot{n}_{\rm ion} = \rho_{\rm UV}\,\xi_{\rm ion}\,f_{\rm esc}$, where $\rho_{\rm UV}$ is the integral of the UV luminosity function (Robertson et al. 2013). Observations indicate that the average galaxy population in reasonably complete samples down to $M_{\rm UV} \approx -17$ at $z \gtrsim 6$ exhibits $\log(\xi_{\rm ion}/{\rm Hz\,erg^{-1}}) \simeq 25.2$–$25.3$ (e.g., Choustikov et al. 2024; Mascia et al. 2024; Simmonds et al. 2024a; Pahl et al. 2025; Begley et al. 2026), which is consistent with or only marginally higher than pre-JWST canonical values (e.g., Robertson et al. 2015). For these $\xi_{\rm ion}$, reionization models typically require population-averaged escape fractions of $f_{\rm esc} \simeq 10$–20% (Robertson et al. 2015), which is broadly supported by inferences using indirect LyC indicators (Mascia et al. 2023; Jaskot et al. 2024b; Jecmen et al. 2026), but with large scatter and sensitive to assumptions about the faint-end slope and cutoff of the UV luminosity function (e.g., Finkelstein et al. 2019; Korber et al. 2026). For simplicity, we adopted a fiducial scenario in which reionization is sustained by an averaged galaxy population characterized by $f_{\rm esc} = 15\%$ and $\log(\xi_{\rm ion}/{\rm Hz\,erg^{-1}}) = 25.25$.

We now consider a simple illustrative scenario in which the ionizing budget is fully dominated by sources similar to U37126. Owing to their exceptionally high $\xi_{\rm ion}$ and near-unity $f_{\rm esc}$, such systems might contribute disproportionately to $\dot{n}_{\rm ion}$ even though they are rare. Requiring the ionizing emissivity contributed by these extreme sources to match that of the fiducial galaxy population yields

$$\left(\frac{f_{\rm esc}}{15\%}\right)\left(\frac{\xi_{\rm ion}}{10^{25.25}}\right) = f_N \left(\frac{f_{\rm esc}}{\geq 86\%}\right)\left(\frac{\xi_{\rm ion}}{10^{25.75}}\right),$$

where f_N is the fraction of such extreme sources relative to the total galaxy population. Adopting the properties inferred for U37126, $\log(\xi_{\rm ion}/{\rm Hz\,erg^{-1}}) \simeq 25.75$ and $f_{\rm esc} \geq 86\%$ (3σ; Section 3), we find $f_N \lesssim 6\%$.

While this scenario is intentionally simplistic, implicitly assuming that such extreme values of $\xi_{\rm ion}$ and $f_{\rm esc}$ are independent of UV luminosity and populate the full luminosity function, it nevertheless illustrates that even a tiny fraction of powerful ionizing sources such as U37126 might contribute significantly, or might even dominate the ionizing photon budget during reionization. This picture is consistent with the results of Papovich et al. (2026), who reported that the majority ($\simeq$82%) of galaxies at $z \simeq 5$–8 exhibit negligible LyC escape ($f_{\rm esc} < 1\%$), while only a small subset are strong LyC emitters, suggesting a highly bimodal distribution in $f_{\rm esc}$ where reionization might be driven by rare but efficient leakers.

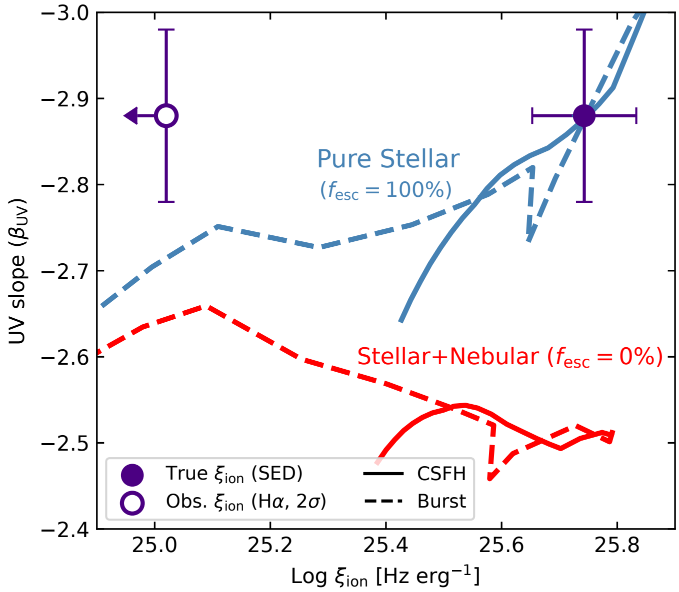

Fig. 8. Relation between the UV slope ($\beta_{\rm UV}$) and the ionizing photon production efficiency ($\xi_{\rm ion}$) for stellar population synthesis models with (red) and without (blue) the contribution of nebular emission, i.e., representing the extreme cases of $f_{\rm esc} = 0$ and $f_{\rm esc} = 1$, respectively. The filled and open circles indicate $\xi_{\rm ion}$ derived from the SED fitting and from the Hα flux limit assuming $f_{\rm esc} = 0$, respectively.

In this regard, recent JWST observations have revealed a progressive steepening of UV slopes with increasing redshift (e.g., Topping et al. 2022; Cullen et al. 2024; Austin et al. 2025; Dottorini et al. 2025), with several sources at $z \gtrsim 6$ exhibiting extremely blue continua ($\beta_{\rm UV} < -2.8$). As illustrated in Fig. 8, such UV slopes require very young stellar populations, implying elevated ionizing photon production efficiencies, $\xi_{\rm ion} \gtrsim 10^{25.6}\,{\rm Hz\,erg^{-1}}$, together with high LyC escape fractions ($f_{\rm esc} \gtrsim 50\%$; see Fig. 3). Moreover, the statistical analysis of Topping et al. (2024b) identified a small but non-negligible fraction ($\simeq$3.4%) of high-redshift sources with $\beta_{\rm UV} < -2.8$ and indications of weak nebular emission, closely resembling U37126, which is comparable to the $f_N \lesssim 6\%$ of extreme LyC emitters required in our illustrative scenario. If spectroscopically confirmed, such systems might already account for a substantial fraction ($\gtrsim$50%) of the total ionizing photon budget during cosmic reionization.

5. Summary and conclusions

We have presented very deep ($\simeq$11 h on-source) JWST/MIRI LRS rest-frame optical spectroscopy of U37126, a $M_{\rm UV} = -20.10$ mildly lensed ($\mu \sim 2.2$) galaxy at $z = 10.255$ previously identified with NIRSpec spectroscopy by Fujimoto et al. (2024). The source exhibits an exceptionally steep UV continuum slope, $\beta_{\rm UV} \simeq -2.9$, a weak Balmer break, a sharp Lyman-α break, and intrinsically faint nebular emission. Despite the clear detection of the continuum in the NIRSpec/PRISM and MIRI/LRS spectra, no recombination or metal emission lines are detected. We derived stringent 3σ rest-frame equivalent width upper limits of $\leq$64 Å, $\leq$174 Å, and $\leq$400 Å for Hβ, [O III] λ5008, and Hα, respectively.

Combining these observational constraints with synthetic stellar population models, we showed that the spectral properties of U37126 require extremely young stellar ages and a very high Lyman-continuum escape fraction. Our results indicate ages ≤2 Myr for instantaneous bursts or ≤10 Myr for constant star formation, implying a very high ionizing photon production efficiency ($\log(\xi_{\rm ion}/{\rm Hz\,erg^{-1}}) \geq 25.6$). From the H$\alpha$ luminosity limit, we derived a conservative lower limit of $f_{\rm esc} \geq 86\%$ (3σ), while an independent SED fitting favored $f_{\rm esc} = 0.94 \pm 0.06$.

U37126 is extremely compact, with a delensed effective radius of $r_{\rm eff} \simeq 61$ pc. The best-fit SED yields a (delensed) stellar mass of $M_\star \simeq 10^{7.8}\,M_\odot$ and a star formation rate SFR $\simeq 10\,M_\odot\,{\rm yr^{-1}}$. This yields very high stellar mass and star-formation-rate surface densities of $\log(\Sigma_{M_\star}/M_\odot\,{\rm pc^{-2}}) \simeq 3.4$ and $\log(\Sigma_{\rm SFR}/M_\odot\,{\rm yr^{-1}\,kpc^{-2}}) \simeq 2.6$, respectively, which are only comparable to those found in young massive star clusters and the most extreme sources at the highest redshifts.

Together with the lack of detectable nebular emission, these properties suggest that U37126 is undergoing an ISM-free starburst phase, in which the ISM is strongly depleted and only a small fraction of ionizing photons are reprocessed by surrounding gas. These conditions may result from an extremely efficient gas-to-star conversion and/or strong feedback that has efficiently cleared the ISM from its stellar core. While our results indicate that LyC photons escape efficiently from the ISM of U37126, recent constraints on the neutral hydrogen column density from the Lyα break ($\log(N_{\rm HI}/{\rm cm^{-2}}) = 19.2 \pm 1.5$) indicated that substantial neutral gas may still be present along the line of sight. Therefore, while our observations favor a very high escape fraction from the galaxy itself, it remains unclear whether the escaping LyC radiation has already reached and ionized its surrounding environment on larger scales.

Although systems such as U37126 are likely rare, their extreme properties that combine a high production and escape of LyC photons suggest that they might contribute disproportionately to the ionizing photon budget during cosmic reionization. Even a small fraction of such sources (~3–6%) can account for a substantial share (~50–100%) of the required ionizing emissivity. This scenario is consistent with emerging JWST evidence of increasingly blue UV continua and weak nebular emission among galaxies with the highest redshifts. If confirmed in larger statistical samples, compact highly efficient LyC emitters such as U37126 may represent a key population for driving and sustaining cosmic reionization.

Acknowledgements. We thank the anonymous referee for the useful comments and suggestions. This work is based on observations made with the NASA/ESA/CSA James Webb Space Telescope. The data were obtained from the Mikulski Archive for Space Telescopes at the Space Telescope Science Institute, which is operated by the Association of Universities for Research in Astronomy, Inc., under NASA contract NAS 5-03127 for JWST. These observations are associated with program #8051. J.A.-M., C.P.-J., B.R.P. acknowledge support from grant PID2024-158856NA-I00, J.A.-M., L.C., C.P.-J., B.R.P. acknowledge support from grant PID2021-127718NB-100, P.G.P.-G. acknowledges support from grant PID2022-139567NB-I00 from the Spanish Ministry of Science and Innovation/State Agency of Research MCIN/AEI/10.13039/501100011033 and by "ERDF A way of making Europe". J.A.-M., L.C., C.P.-J., B.R.P., P.G.P.-G. acknowledge support by grant CSIC/BILATERALES2025/BIJSP25022. M.C. acknowledges INAF GO Grant 2024 "Revealing the nature of bright galaxies at cosmic dawn with deep JWST spectroscopy". T.H. was supported by JSPS KAKENHI 25K00020. Y.H. acknowledges support from the Japan Society for the Promotion of Science (JSPS) Grant-in-Aid for Scientific Research (24H00245), the JSPS Core-to-Core Program (JPJSCCA20210003), and the JSPS International Leading Research (22K21349). Y.F. is supported by JSPS KAKENHI Grant Numbers JP22K21349 and JP23K13149. D.L. was supported by research grants (VIL16599,VIL54489) from VILLUM FONDEN. P.S. acknowledges support from INAF RF2024 Large Grant "UNDUST: UNveiling the Dawn of the Universe with JWST" The data were obtained from the Mikulski Archive for Space Telescopes at the Space Telescope Science Institute, which is operated by the Association of Universities for Research in Astronomy, Inc., under NASA contract NAS 5-03127 for *JWST*; and from the European *JWST* archive (e*JWST*) operated by the ESDC. This research made use of Photutils, an Astropy package for detection and photometry of astronomical sources (Bradley et al. 2022).

References

Algera, H. S. B., Weaver, J. R., Bakx, T. J. L. C., et al. 2025, Open J. Astrophys., submitted [arXiv:2512.14486]
Álvarez-Márquez, J., Colina, L., Crespo Gómez, A., et al. 2024, A&A, 686, A85
Álvarez-Márquez, J., Crespo Gómez, A., Colina, L., et al. 2025, A&A, 695, A250
Álvarez-Márquez, J., Colina, L., Crespo-Gomez, A., et al. 2026, A&A, submitted [arXiv:2602.02323]
Arrabal Haro, P., Dickinson, M., Finkelstein, S. L., et al. 2023, Nature, 622, 707
Atek, H., Chemerynska, I., Wang, B., et al. 2023, MNRAS, 524, 5486
Austin, D., Conselice, C. J., Adams, N. J., et al. 2025, ApJ, 995, 43
Baker, W. M., D'Eugenio, F., Maiolino, R., et al. 2025, A&A, 697, A90
Begley, R., McLure, R. J., Cullen, F., et al. 2026, MNRAS, 545, staf1995
Bergvall, N., Leitet, E., Zackrisson, E., & Marquart, T. 2013, A&A, 554, A38
Bezanson, R., Labbe, I., Whitaker, K. E., et al. 2024, ApJ, 974, 92
Bhatawdekar, R., & Conselice, C. J. 2021, ApJ, 909, 144
Boquien, M., Burgarella, D., Roehlly, Y., et al. 2019, A&A, 622, A103
Bouwens, R. J., Illingworth, G. D., Oesch, P. A., et al. 2010, ApJ, 708, L69
Bouwens, R. J., Illingworth, G. D., Oesch, P. A., et al. 2012, ApJ, 754, 83
Bouwens, R. J., Illingworth, G. D., Oesch, P. A., et al. 2014, ApJ, 793, 115
Boyett, K., Trenti, M., Leethochawalit, N., et al. 2024, Nat. Astron., 8, 657
Bradley, L., Sipőcz, B., Robitaille, T., et al. 2022, https://doi.org/10.5281/zenodo.6825092
Bruzual, G., & Charlot, S. 2003, MNRAS, 344, 1000
Bunker, A. J., Saxena, A., Cameron, A. J., et al. 2023, A&A, 677, A88
Burgarella, D., Buat, V., & Iglesias-Páramo, J. 2005, MNRAS, 360, 1413
Burgarella, D., Buat, V., Theulé, P., et al. 2025, A&A, 699, A336
Bushouse, H., Eisenhamer, J., Dencheva, N., et al. 2025, https://doi.org/10.5281/zenodo.17515973
Calabrò, A., Castellano, M., Zavala, J. A., et al. 2024, ApJ, 975, 245
Calzetti, D., Kinney, A. L., & Storchi-Bergmann, T. 1994, ApJ, 429, 582
Calzetti, D., Armus, L., Bohlin, R. C., et al. 2000, ApJ, 533, 682
Cardelli, J. A., Clayton, G. C., & Mathis, J. S. 1989, ApJ, 345, 245
Carniani, S., Hainline, K., D'Eugenio, F., et al. 2024, Nature, 633, 318
Castellano, M., Fontana, A., Treu, T., et al. 2022, ApJ, 938, L15
Castellano, M., Napolitano, L., Fontana, A., et al. 2024, ApJ, 972, 143
Chabrier, G. 2003, PASP, 115, 763
Chemerynska, I., Atek, H., Furtak, L. J., et al. 2026, MNRAS, 546, staf2267
Chisholm, J., Saldana-Lopez, A., Flury, S., et al. 2022, MNRAS, 517, 5104
Choustikov, N., Katz, H., Saxena, A., et al. 2024, MNRAS, 529, 3751
Crespo Gómez, A., Tamura, Y., Colina, L., et al. 2025, A&A, submitted [arXiv:2511.14658]
Cullen, F., McLure, R. J., McLeod, D. J., et al. 2023, MNRAS, 520, 14
Cullen, F., McLeod, D. J., McLure, R. J., et al. 2024, MNRAS, 531, 997
Curtis-Lake, E., Carniani, S., Cameron, A., et al. 2023, Nat. Astron., 7, 622
de Barros, S., Vanzella, E., Amorín, R., et al. 2016, A&A, 585, A51
Dekel, A., Sarkar, K. C., Birnboim, Y., Mandelker, N., & Li, Z. 2023, MNRAS, 523, 3201
Dessauges-Zavadsky, M., Marques-Chaves, R., Schaerer, D., et al. 2025, A&A, 693, A17
Donnan, C. T., Dickinson, M., Taylor, A. J., et al. 2025, ApJ, 993, 224
Donnan, C. T., McLeod, D. J., McLure, R. J., et al. 2026, ApJ, 1002, 134
Dottorini, D., Calabrò, A., Pentericci, L., et al. 2025, A&A, 698, A234
Ferrara, A., Pallottini, A., & Dayal, P. 2023, MNRAS, 522, 3986
Ferrara, A., Giavalisco, M., Pentericci, L., et al. 2025, Open J. Astrophys., 8, 125
Finkelstein, S. L., Papovich, C., Salmon, B., et al. 2012, ApJ, 756, 164
Finkelstein, S. L., D'Aloisio, A., Paardekooper, J.-P., et al. 2019, ApJ, 879, 36
Fiore, F., Ferrara, A., Bischetti, M., Feruglio, C., & Travascio, A. 2023, ApJ, 943, L27
Flury, S. R., Jaskot, A. E., Ferguson, H. C., et al. 2022, ApJ, 930, 126
Fujimoto, S., Wang, B., Weaver, J. R., et al. 2024, ApJ, 977, 250
Furtak, L. J., Zitrin, A., Weaver, J. R., et al. 2023, MNRAS, 523, 4568
Giovinazzo, E., Oesch, P. A., Weibel, A., et al. 2026, A&A, 707, A352
Goulding, A. D., Greene, J. E., Setton, D. J., et al. 2023, ApJ, 955, L24
Hainline, K. N., D'Eugenio, F., Jakobsen, P., et al. 2024, ApJ, 976, 160
Harikane, Y., Ouchi, M., Oguri, M., et al. 2023, ApJS, 265, 5
Harikane, Y., Nakajima, K., Ouchi, M., et al. 2024, ApJ, 960, 56
Harikane, Y., Inoue, A. K., Ellis, R. S., et al. 2025, ApJ, 980, 138
Harikane, Y., Perez-Gonzalez, P. G., Alvarez-Marquez, J., et al. 2026, ArXiv e-prints [arXiv:2601.21833]
Heintz, K. E., Watson, D., Brammer, G., et al. 2024, Science, 384, 890
Helton, J. M., Morrison, J. E., Hainline, K. N., et al. 2026, ApJ, 1004, L30
Hsiao, T. Y.-Y., Álvarez-Márquez, J., Coe, D., et al. 2024, ApJ, 973, 81
Inoue, A. K. 2010, MNRAS, 401, 1325
Isobe, Y., Ouchi, M., Nakajima, K., et al. 2023, ApJ, 956, 139
Izotov, Y. I., Schaerer, D., Thuan, T. X., et al. 2016, MNRAS, 461, 3683
Izotov, Y. I., Worseck, G., Schaerer, D., et al. 2018, MNRAS, 478, 4851

Izotov, Y. I., Schaerer, D., Worseck, G., et al. 2025, A&A, 704, A19
Jaskot, A. E., Silveyra, A. C., Plantinga, A., et al. 2024a, ApJ, 972, 92
Jaskot, A. E., Silveyra, A. C., Plantinga, A., et al. 2024b, ApJ, 973, 111
Jecmen, M. C., Chisholm, J., Atek, H., et al. 2026, ApJ, 1001, 234
Katz, H., Cameron, A. J., Saxena, A., et al. 2025, Open J. Astrophys., 8, 104
Kendrew, S., Scheithauer, S., Bouchet, P., et al. 2015, PASP, 127, 623
Kerutt, J., Oesch, P. A., Wisotzki, L., et al. 2024, A&A, 684, A42
Kim, K. J., Bayliss, M. B., Rigby, J. R., et al. 2023, ApJ, 955, L17
Komarova, L., Oey, M. S., Marques-Chaves, R., et al. 2025, ApJ, 994, 192
Korber, D., Schaerer, D., Marques-Chaves, R., et al. 2026, A&A, 710, L15
Kuruvanthodi, A., Schaerer, D., Marques-Chaves, R., et al. 2024, A&A, 691, A310
Leitherer, C., Schaerer, D., Goldader, J. D., et al. 1999, ApJS, 123, 3
Li, Z., Dekel, A., Sarkar, K. C., et al. 2024, A&A, 690, A108
Looser, T. J., D'Eugenio, F., Maiolino, R., et al. 2024, Nature, 629, 53
Luridiana, V., Morisset, C., & Shaw, R. A. 2015, A&A, 573, A42
Marques-Chaves, R., Schaerer, D., Álvarez-Márquez, J., et al. 2021, MNRAS, 507, 524
Marques-Chaves, R., Schaerer, D., Álvarez-Márquez, J., et al. 2022, MNRAS, 517, 2972
Marques-Chaves, R., Schaerer, D., Vanzella, E., et al. 2024, A&A, 691, A87
Marques-Chaves, R., Schaerer, D., Dessauges-Zavadsky, M., et al. 2026, A&A, 711, A112
Mascia, S., Pentericci, L., Calabrò, A., et al. 2023, A&A, 672, A155
Mascia, S., Pentericci, L., Calabrò, A., et al. 2024, A&A, 685, A3
Mason, C. A., Chen, Z., Stark, D. P., et al. 2026, A&A, 705, A114
Menon, S. H., Burkhart, B., Somerville, R. S., Thompson, T. A., & Sternberg, A. 2025, ApJ, 987, 12
Messa, M., Vanzella, E., Loiacono, F., et al. 2025, A&A, 694, A59
Morales, A. M., Finkelstein, S. L., Leung, G. C. K., et al. 2024, ApJ, 964, L24
Morishita, T., Stiavelli, M., Chary, R.-R., et al. 2024, ApJ, 963, 9
Naidu, R. P., Tacchella, S., Mason, C. A., et al. 2020, ApJ, 892, 109
Naidu, R. P., Oesch, P. A., Brammer, G., et al. 2026, Open J. Astrophys., 9, 56033
Napolitano, L., Castellano, M., Pentericci, L., et al. 2025, A&A, 693, A50
Newville, M., Otten, R., Nelson, A., et al. 2025, https://doi.org/10.5281/zenodo.15014437
Osterbrock, D. E., & Ferland, G. J. 2006, Astrophysics of Gaseous Nebulae and Active Galactic Nuclei
Pahl, A., Topping, M. W., Shapley, A., et al. 2025, ApJ, 981, 134
Papovich, C., Cole, J. W., Hu, W., et al. 2026, ApJ, 1000, 111
Pasha, I., & Miller, T. B. 2023, J. Open Source Softw., 8, 5703
Pérez-González, P. G., Costantin, L., Langeroodi, D., et al. 2023, ApJ, 951, L1
Perrin, M. D., Sivaramakrishnan, A., Lajoie, C.-P., et al. 2014, SPIE Conf. Ser., 9143, 91433X
Planck Collaboration VI. 2020, A&A, 641, A6
Price, S. H., Bezanson, R., Labbe, I., et al. 2025, ApJ, 982, 51
Reddy, N. A., Sanders, R. L., Shapley, A. E., et al. 2023a, ApJ, 951, 56
Reddy, N. A., Topping, M. W., Sanders, R. L., Shapley, A. E., & Brammer, G. 2023b, ApJ, 952, 167
Rieke, G. H., Wright, G. S., Böker, T., et al. 2015, PASP, 127, 584
Rivera-Thorsen, T. E., Dahle, H., Chisholm, J., et al. 2019, Science, 366, 738
Roberts-Borsani, G., Oesch, P. A., Ellis, R., et al. 2026, MNRAS, 548, stag701
Robertson, B. E., Furlanetto, S. R., Schneider, E., et al. 2013, ApJ, 768, 71
Robertson, B. E., Ellis, R. S., Furlanetto, S. R., & Dunlop, J. S. 2015, ApJ, 802, L19
Saxena, A., Cameron, A. J., Katz, H., et al. 2026, MNRAS, 548, stag808
Schaerer, D., Guibert, J., Marques-Chaves, R., & Martins, F. 2025, A&A, 693, A271
Sharma, M., Theuns, T., Frenk, C., et al. 2017, MNRAS, 468, 2176
Simmonds, C., Tacchella, S., Hainline, K., et al. 2024a, MNRAS, 527, 6139
Simmonds, C., Verhamme, A., Inoue, A. K., et al. 2024b, MNRAS, 530, 2133
Stanway, E. R., & Eldridge, J. J. 2018, MNRAS, 479, 75
Steidel, C. C., Bogosavljević, M., Shapley, A. E., et al. 2018, ApJ, 869, 123
Stiavelli, M., Morishita, T., Chiaberge, M., et al. 2023, ApJ, 957, L18
Suess, K. A., Weaver, J. R., Price, S. H., et al. 2024, ApJ, 976, 101
Tacchella, S., Eisenstein, D. J., Hainline, K., et al. 2023, ApJ, 952, 74
Tang, M., Stark, D. P., Mason, C. A., et al. 2026, ApJ, 1001, 38
Topping, M. W., Stark, D. P., Endsley, R., et al. 2022, ApJ, 941, 153
Topping, M. W., Stark, D. P., Endsley, R., et al. 2024a, MNRAS, 529, 4087
Topping, M. W., Stark, D. P., Senchyna, P., et al. 2024b, MNRAS, 529, 3301
Vanzella, E., de Barros, S., Vasei, K., et al. 2016, ApJ, 825, 41
Vanzella, E., Claeyssens, A., Welch, B., et al. 2023, ApJ, 945, 53
Weaver, J. R., Cutler, S. E., Pan, R., et al. 2024, ApJS, 270, 7
Weibel, A., Oesch, P. A., Barrufet, L., et al. 2024, MNRAS, 533, 1808
Wright, G. S., Wright, D., Goodson, G. B., et al. 2015, PASP, 127, 595
Wright, G. S., Rieke, G. H., Glasse, A., et al. 2023, PASP, 135, 048003
Yanagisawa, H., Ouchi, M., Nakajima, K., et al. 2025, ApJ, 988, 86
Zackrisson, E., Inoue, A. K., & Jensen, H. 2013, ApJ, 777, 39
Zackrisson, E., Binggeli, C., Finlator, K., et al. 2017, ApJ, 836, 78
Zavala, J. A., Castellano, M., Akins, H. B., et al. 2025, Nat. Astron., 9, 155

[1] Geneva Observatory, Department of Astronomy, University of Geneva, Chemin Pegasi 51, CH-1290 Versoix, Switzerland
[2] Centro de Astrobiología (CAB), CSIC-INTA, Ctra. de Ajalvir km 4, Torrejón de Ardoz E-28850, Madrid, Spain
[3] European Space Agency (ESA), ESA Office, Space Telescope Science Institute, 3700 San Martin Drive, Baltimore, MD 21218, USA
[4] Department of Astronomy, Indiana University, 727 East Third Street, Bloomington, IN 47405, USA
[5] Departamento de Física de la Tierra y Astrofísica, Facultad de Ciencias Físicas, Universidad Complutense de Madrid, E-28040 Madrid, Spain
[6] Leiden Observatory, Leiden University, PO Box 9513, NL-2300 RA Leiden, The Netherlands
[7] INAF – Osservatorio Astronomico di Roma, Via Frascati 33, 00078 Monteporzio Catone, Italy
[8] Kapteyn Astronomical Institute, University of Groningen, P.O. Box 800, 9700AV Groningen, The Netherlands
[9] Space Telescope Science Institute (STScI), 3700 San martin Drive, Baltimore, MD 21218, USA
[10] Center for Frontier Science, Chiba University, 1-33 Yayoi-cho, Inage-ku, Chiba 263-8522, Japan
[11] David A. Dunlap Department of Astronomy and Astrophysics, University of Toronto, 50 St. George Street, Toronto, Ontario M5S 3H4, Canada
[12] Dunlap Institute for Astronomy and Astrophysics, 50 St. George Street, Toronto, Ontario M5S 3H4, Canada
[13] Institute for Cosmic Ray Research, The University of Tokyo, 5-1-5 Kashiwanoha, Kashiwa, Chiba 277-8582, Japan
[14] Division of Physics, Faculty of Pure and Applied Sciences, University of Tsukuba, Tsukuba, Ibaraki 305-8571, Japan
[15] Tomonaga Center for the History of the Universe (TCHoU), Faculty of Pure and Applied Sciences, University of Tsukuba, Tsukuba, Ibaraki 305-8571, Japan
[16] Department of Astronomy, University of Texas, Austin, TX 78712, USA
[17] Institute of Science and Technology Austria (ISTA), Am Campus 1, 3400 Klosterneuburg, Austria
[18] Department of Physics, School of Advanced Science and Engineering, Faculty of Science and Engineering, Waseda University, 3-4-1 Okubo, Shinjuku, Tokyo 169-8555, Japan
[19] Waseda Research Institute for Science and Engineering, Faculty of Science and Engineering, Waseda University, 3-4-1 Okubo, Shinjuku, Tokyo 169-8555, Japan
[20] DARK, Niels Bohr Institute, University of Copenhagen, Jagtvej 155A, 2200 Copenhagen, Denmark
[21] University of Massachusetts Amherst, 710 North Pleasant Street, Amherst, MA 01003-9305, USA
[22] Department of Astronomy, Stockholm University, Oscar Klein Centre, AlbaNova University Centre, 106 91 Stockholm, Sweden
[23] AURA for the European Space Agency (ESA), Space Telescope Science Institute, 3700 San Martin Dr., Baltimore, MD 21218, USA
[24] UK Astronomy Technology Centre, Royal Observatory Edinburgh, Blackford Hill, Edinburgh EH9 3HJ, UK

Appendix A: BPASS predictions for different metallicities

Figures A.1, A.2, A.3, and A.4 show the model predictions of the UV slope, EW_0 (Hα) and the Balmer break strength as a function of age (top) and their combination (bottom) for stellar metallicities of $Z = Z_\odot$, $Z/Z_\odot = 50\%$, $Z/Z_\odot = 5\%$, and $Z/Z_\odot = 0.5\%$, respectively.

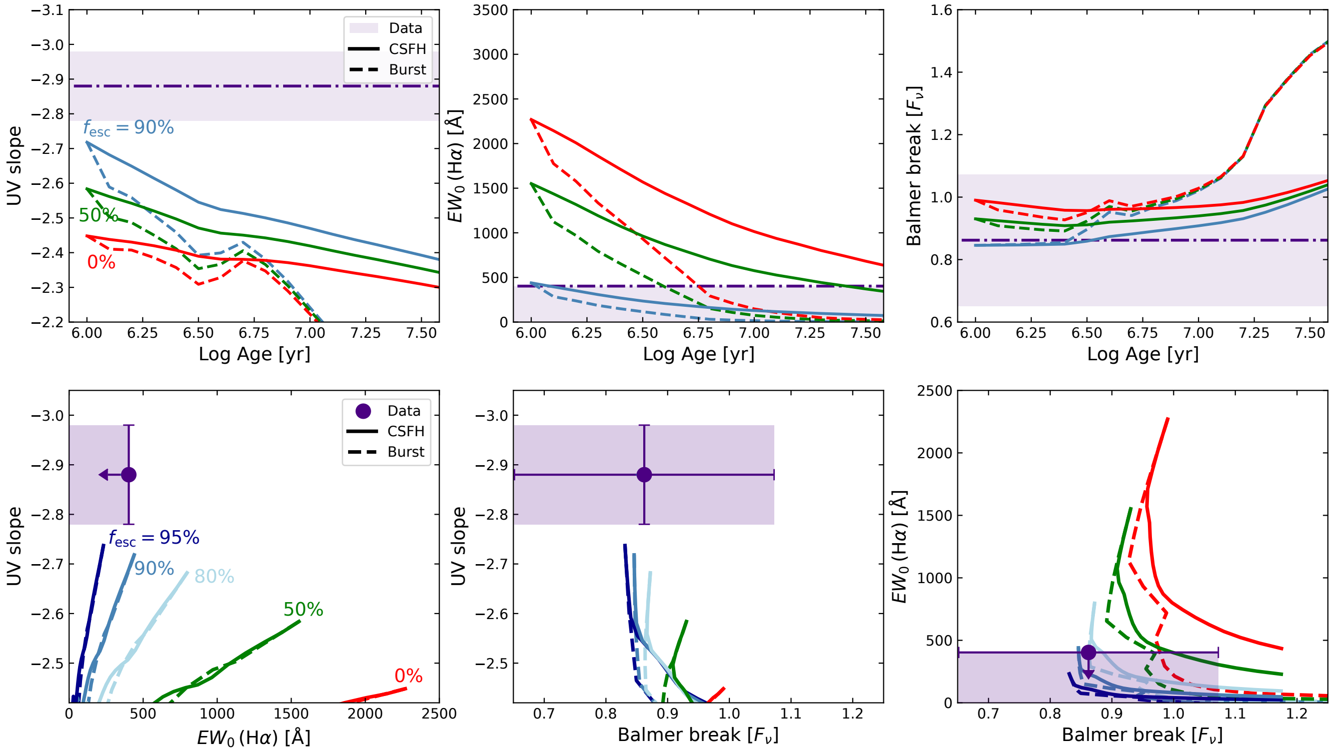

Fig. A.1. Same as Figure 3 but for BPASS models with stellar metallicity of $Z = 0.02$ (or $Z/Z_\odot = 100\%$).

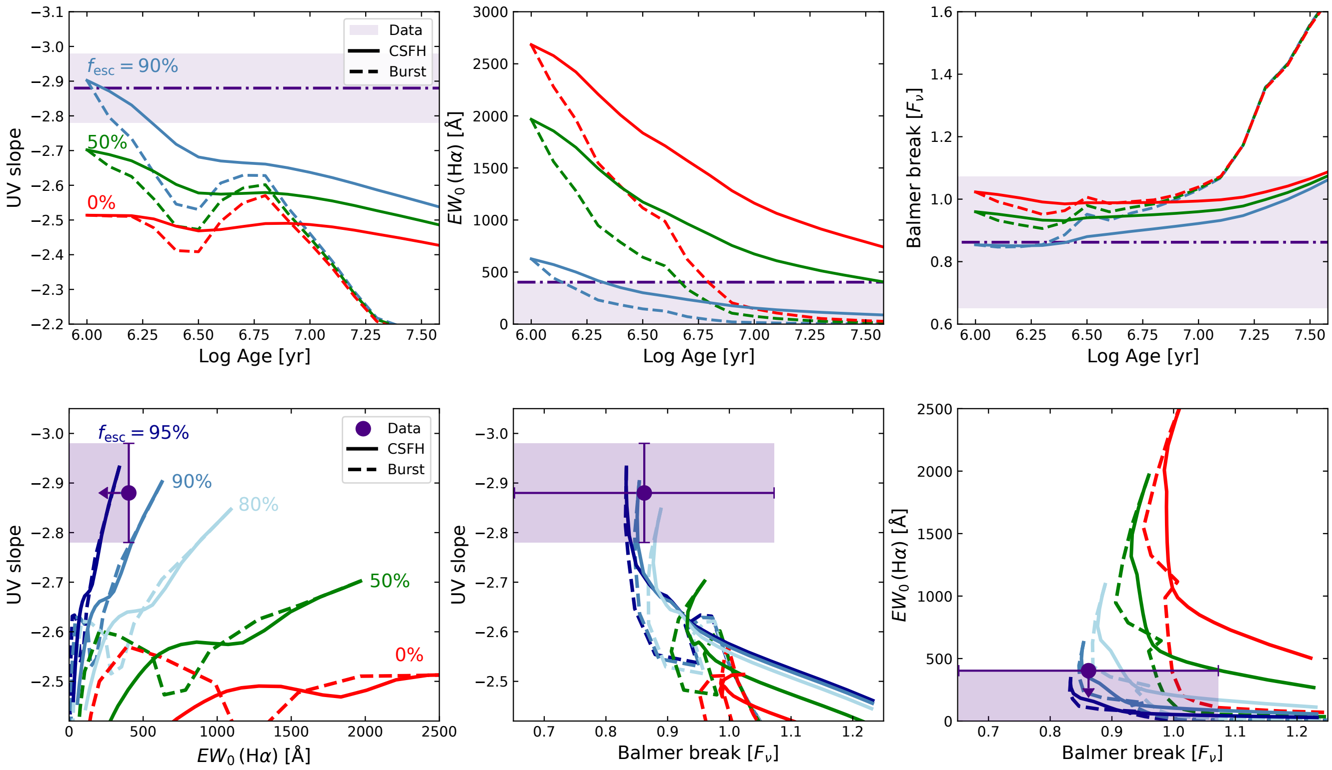

Fig. A.2. Same as Figure 3 but for BPASS models with stellar metallicity of $Z = 0.01$ (or $Z/Z_\odot = 50\%$).

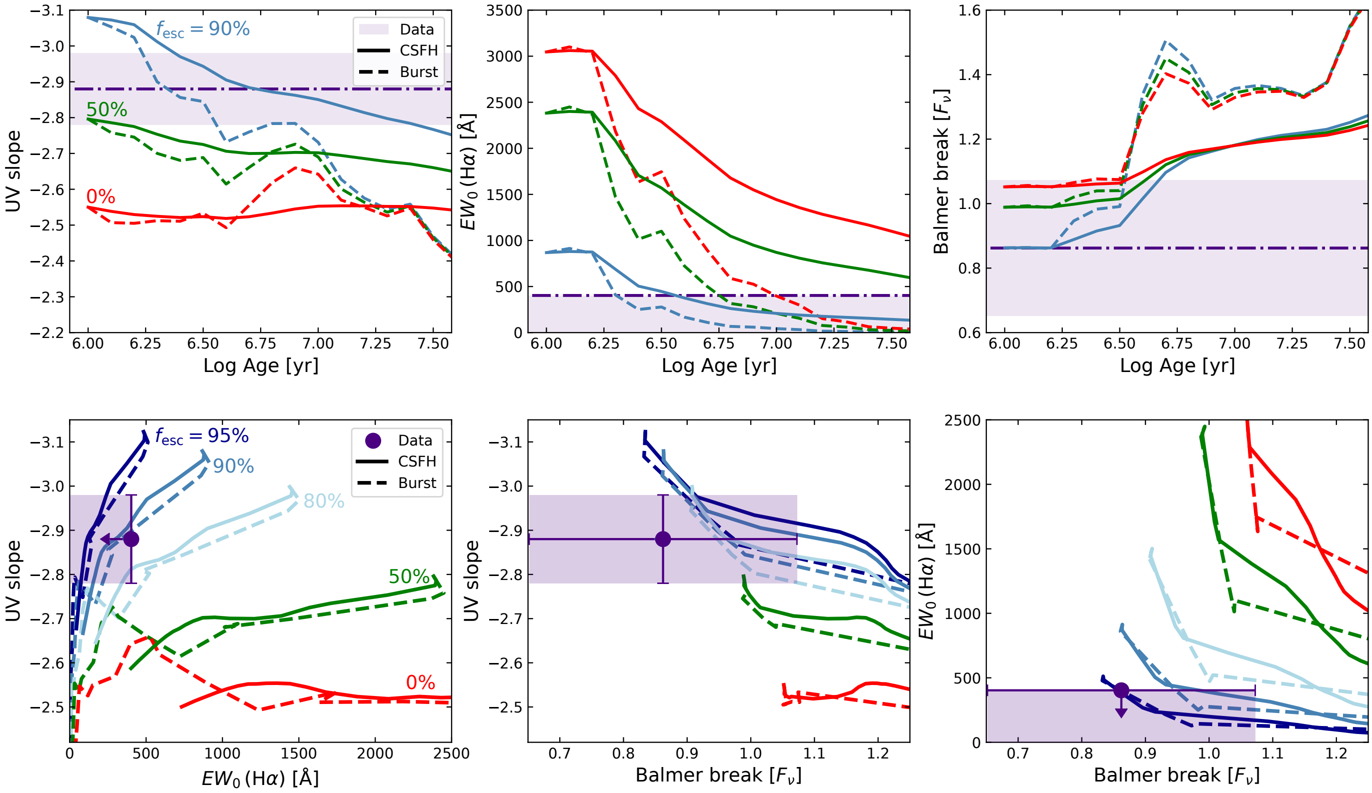

Fig. A.3. Same as Figure 3 but for BPASS models with stellar metallicity of $Z = 0.001$ (or $Z/Z_\odot = 5\%$).

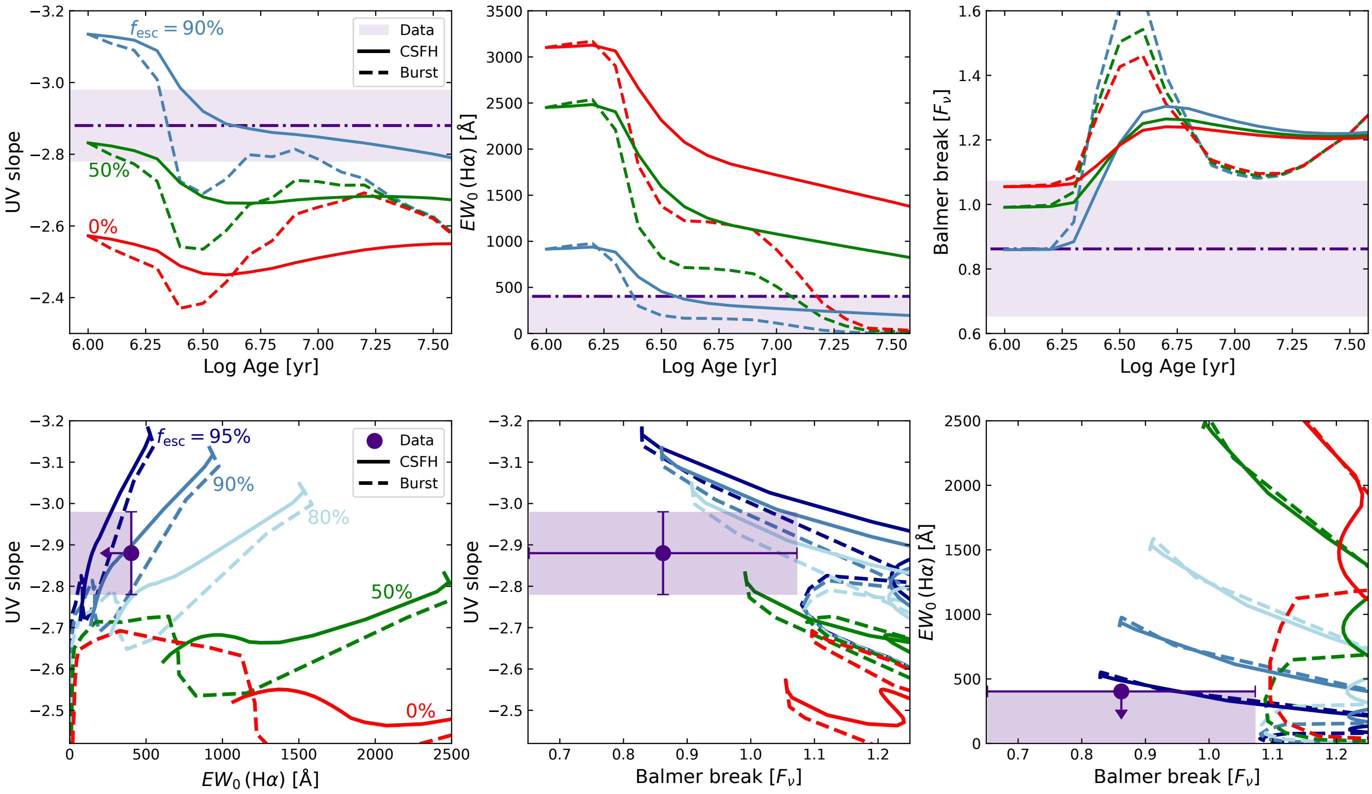

Fig. A.4. Same as Figure 3 but for BPASS models with stellar metallicity of $Z = 0.0001$ (or $Z/Z_\odot = 0.5\%$).